Theor Chem Account (2008) 119:383–405
DOI 10.1007/s00214-007-0395-2

REGULAR ARTICLE

Shift equations iteration solution to *n*-level close coupled equations, and the two-level nonadiabatic tunneling problem revisited

Randall S. Dumont · Stephen W. K. Lam

Received: 12 October 2007 / Published online: 6 November 2007

The shift equations iteration (SEI) solves the *n*-level quantum scattering problem in one dimension, i.e., the close-coupled equations, free from exponential instability arising from closed channels. SEI provides exponential-instability-free transmission and reflection coefficients, and is well suited to two-sided scattering problems such as conduction in molecular wires. Our most efficient implementation of SEI utilizes an adaptation of the log-derivative symplectic integrator described by Manolopoulos and Gray in (J Chem Phys 102:9214, 1995). The two-level nonadiabatic tunneling system is investigated—in the tunneling regime, above the barrier, and at resonance. Nonadiabatic components in the upper channel wavefunction (and lower channel wavefunction at resonance energies) are found to be non-adiabatic, i.e., not describable by WKB functions. Their behavior is characterized in terms of an empirical model relating these components to adiabatic components in the lower (upper) channel and the potential energy coupling.

1 Introduction

We present a new numerical method, which we term the shift equations iteration (SEI), for solving the *n*-level quantum scattering problem in one dimension, i.e., the close-coupled equations.[1] It is based on the WKB representation of the first-order form of the Schrödinger equation, and is constructed so as to circumvent the well-known exponential instability arising from closed channels [2–6]. As such, the method competes directly with the log-derivative method [7–10], the de facto standard for integration of close-coupled equations.

Atomic and molecular collision systems provide many examples of *n*-level quantum scattering in one dimension.[2] The *n*-levels could be electronic states, and/or vibrational levels of coordinates orthogonal to the reaction coordinate. Molecular collisions can be treated as one-dimensional systems through the use of hyperspherical coordinates. Examples of such computations include $F + H_2$ reactive scattering [12], related $F + D_2$ studies [13] (a review of the $F + H_2$ reaction is provided by Manolopoulos [14]), and collinear treatments of $D + H_2$ reactivity [15] and CO_2 photodissociation [16]. References [12,16] use the original Johnson [7] log-derivative method, Ref. [13] uses the constant reference potential log-derivative method of Manolopoulos [10], while Ref. [15] uses the R-matrix method [3,4]. The latter method is subject to exponential instability when there are closed channels. In Ref. [16], the close-coupled equations treat an electronic excited state in addition to the vibrational states orthogonal to the reaction coordinate, i.e., the level index includes the electronic state label and the orthogonal vibrational state label. An example of a collision system with account of an electronic excited state is provided by the Ref. [17] study of $H + N_2^+$.

The reaction coordinate in all of the above examples is a radial coordinate. As such, all of the scattering processes these studies investigate appear as multi-channel reflection processes. In this article, the focus is on two-sided scattering systems, such as the model for HN_3 decomposition in Ref. [6], with reflection and transmission processes. Two-sided one-dimensional scattering is a paradigm of molecular

[1] Molecular dynamics theory and experiment are reviewed in [1].

R. S. Dumont (✉) · S. W. K. Lam
Department of Chemistry, McMaster University, 1280 Main St. W. Hamilton, ON, Canada L8S 4M1
e-mail: dumontr@mcmaster.ca

[2] An excellent introduction to molecular scattering is found in [11].

electronics [18–20] and quantum wires [19].[3] Conduction through a nanodevice is treated as a two-sided scattering problem in terms of the Landauer formula [22,23]. It is for two-sided scattering systems that the shift equations iteration offers potential advantage over log-derivative methods. It is explained in Sect. 4 how log-derivative methods generally provide only reflection coefficients free of exponential instability. Transmission coefficients are provided in terms of the wavefunction matrix, or its equivalent, and as such are subject to exponential instability. Nevertheless, Ref [6]. provides a method which limits the exponential instability to exponential decay and demonstrates the method's efficacy for a two level two-sided scattering system. It is not clear how robust the algorithm is in general. We have used it to compute accurate transmission coefficients for three and four level systems [24]. However, it does not appear to provide accurate wavefunction closed channel components. A niche for SEI might be detailed studies of closed channel wavefunction components—such as provided below in Sect. 3.3. Closed channel components are of interest because they are associated with classically forbidden processes and intrinsically quantum phenomena.

The shift equations iteration—derived in Sects. 2 and 3—breaks propagation across the one-dimensional interval into smaller steps such that exponential growth is manageable for each step. It is shown below that, if the steps are not too large, SEI suppresses the accumulation of exponential growth from one step to the next. The rate of convergence of SEI is governed by the accuracy of the underlying integrator used to propagate between neighboring grid points. SEI does not prescribe the underlying integrator. As such, SEI can be combined with any number of existing integrators—either log-derivative integrators normally used to propagate across the entire interval—or other first-order (or adapted second-order) differential equation integrators. The latter are generally subject to exponential instability and cannot otherwise be used to propagate across the entire interval. However, we see, in Sect. 4, that when combined with SEI, these integrators can provide useful, stable computation of the scattering wavefunctions. Nevertheless, our best results, i.e., fastest convergence, are obtained for SEI in combination with the log-derivative form [25] of the fifth-order symplectic integrator of McLachlan and Atela [26]. Manolopoulos and Gray [25] describe the symplectic character of the first-order form of the radial Schrödinger equation and its consequences—specifically, the existence of a set of phase space integral invariants of Poincaré. A symplectic integrator, such as that provided in Ref. [26], exactly conserves (to within rounding error) all of the integral invariants. This significantly improves the reliability of such methods over non-symplectic approaches. However, Manolopoulos and Gray also show that symplectic symmetry is implicitly incorporated into many existing methods. Nevertheless, we adopt the fifth-order integrator of Ref. [25] because it is easy to program, in addition to being very reliable. We have not combined SEI with any other existing log-derivative methods.

In Sect. 4, the classic two-level nonadiabatic tunneling problem [27] is re-visited. First, we demonstrate the efficacy of SEI together with the fifth order log-derivative symplectic integrator of Ref. [25] (in the tunneling, and above barrier regimes). Then, we investigate the observed reflection and transmission probabilities, and associated wavefunctions. Complete reflection, as described in Ref. [29], is observed exactly at resonance. Specifically, with the resonance energy determined to within double precision accuracy, transmission probability is computed to be at or below 10^{-20}. Nakamura [29] highlights this phenomenon and proposes a molecular switching device based on the effect. Specifically, if the avoided crossing is loose, the transmission probability switches rapidly from near 100 to 0% as energy is scanned across a resonance. Controlling the energy of the transmitting particle (e.g. an electron), within a narrow range, controls with near certainty whether the particle will transmit or not.

Another interesting phenomenon observed is the form of the upper channel wavefunction at non-resonant energies. Specifically, the closed channel component of the wavefunction is found to be non-adiabatic—its decay heading into asymptotic regions is much slower than the fall-off of the corresponding WKB function. These non-adiabatic upper channel wavefunctions are empirically modeled by the lower channel wavefunction weighted with the potential energy coupling (or a variation thereof) in diabatic representation. The non-resonant upper channel wavefunction persists at resonant energies, in superposition with the resonant wavefunction—the pseudo-bound state in the upper channel well. While the former component of the wavefunction is generally quite small, it can be quite broad—in fact, much more so than one might expect from the viewpoint of the adiabatic (i.e., WKB) approximation wherein the tails of the upper channel wavefunction decay much faster than is observed. The unexpected broad base character of the upper channel wavefunctions might play a role in, for example, the interaction of neighboring avoided crossings in subsequent applications.

In Sect. 2, we review the n-level system and the first-order form of the Schrödinger equation. These equations are transformed to adiabatic representation, and then to WKB representation as in Ref. [30] which treats the simple one-level system.

[3] Some recent electronic structure computations for semiconductor quantum dots and wires are provided in Ref. [21].

2 The *n*-level system WKB representation

We consider an n-level system initially in "diabatic representation". The system wavefunction is an n component vector function, $\Psi(x)$, of the "reaction coordinate", x, subject to a Hamiltonian of the form,

$$\hat{\mathsf{H}} = \frac{-\hbar^2}{2m}\frac{\mathrm{d}^2}{\mathrm{d}x^2}\mathsf{1} + \mathsf{V}(x). \tag{1}$$

The kinetic energy matrix is isotropic and diagonal, in diabatic representation. $\mathsf{1}$ is the $n \times n$ identity matrix. Coupling between levels is manifest in the off-diagonal elements of the potential matrix, $\mathsf{V}(x)$. In general, the potential matrix is complex symmetric (real symmetric on the real x axis), and is diagonalized by orthogonal transformation,

$$\mathsf{Z}^{-1}(x)\,\mathsf{V}(x)\,\mathsf{Z}(x) = \mathsf{v}(x).$$

$\mathsf{Z}(x)$ is orthogonal for all x. We adopt the convention that the eigenvalues—the elements of $\mathsf{v}(x)$—appear in ascending order for real x. The non-crossing rule [31] (we assume that $\mathsf{V}(x)$ is irreducible) for eigenvalues ensures that this order is maintained for all real x if it is imposed for one real x.

The WKB approximation to the solutions of the above time-independent Schrödinger equation arises naturally as an adiabatic approximation in the limit of slowly varying $\mathsf{V}(x)$ [32]. This approximation is conveniently derived via the first-order form of the Schrödinger equation,

$$\begin{pmatrix}\Psi(x)\\ \Psi'(x)\end{pmatrix}' = \begin{pmatrix}0 & 1\\ -\mathsf{P}^2(x)/\hbar^2 & 0\end{pmatrix}\begin{pmatrix}\Psi(x)\\ \Psi'(x)\end{pmatrix}. \tag{2}$$

The prime superscript here denotes derivative with respect to x, and

$$\mathsf{P}^2(x) = 2m\left[E\mathsf{1} - \mathsf{V}(x)\right]$$

is the square momentum matrix in diabatic representation. As in the derivation of the WKB representation for a one-level system ($n = 1$) [30], we introduce the transformation to adiabatic representation,

$$\begin{pmatrix}\Psi(x)\\ \Psi'(x)\end{pmatrix} = \begin{pmatrix}\mathsf{Z}(x) & \mathsf{Z}(x)\\ \mathrm{i}\mathsf{P}(x)\mathsf{Z}(x)/\hbar & -\mathrm{i}\mathsf{P}(x)\mathsf{Z}(x)/\hbar\end{pmatrix}\begin{pmatrix}\psi_+(x)\\ \psi_-(x)\end{pmatrix}.$$

The $\psi_\pm(x)$ representation defined by this transformation is adiabatic in the sense that its components correspond to right and left-going motions in specific adiabatic levels. In the limit of slow variation of $\mathsf{P}(x)$ and $\mathsf{Z}(x)$, transitions between levels and between right and left-going motion vanish and the equations for the components of $\psi_+(x)$ and $\psi_-(x)$ become separable, varying independently. In terms of the diagonal adiabatic momentum matrix, $\mathsf{p}(x) = \mathsf{Z}^{-1}(x)\,\mathsf{P}(x)\,\mathsf{Z}(x)$, the transformations between adiabatic and diabatic representations take the form,

$$\begin{pmatrix}\Psi(x)\\ \Psi'(x)\end{pmatrix} = \begin{pmatrix}\mathsf{Z}(x) & \mathsf{Z}(x)\\ \mathrm{i}\mathsf{Z}(x)\,\mathsf{p}(x)/\hbar & -\mathrm{i}\mathsf{Z}(x)\,\mathsf{p}(x)/\hbar\end{pmatrix}\begin{pmatrix}\psi_+(x)\\ \psi_-(x)\end{pmatrix} \tag{3}$$

and

$$\begin{pmatrix}\psi_+(x)\\ \psi_-(x)\end{pmatrix} = \frac{1}{2}\begin{pmatrix}\mathsf{Z}^{-1}(x) & -\mathrm{i}\hbar\mathsf{p}^{-1}(x)\,\mathsf{Z}^{-1}(x)\\ \mathsf{Z}^{-1}(x) & \mathrm{i}\hbar\mathsf{p}^{-1}(x)\,\mathsf{Z}^{-1}(x)\end{pmatrix}\begin{pmatrix}\Psi(x)\\ \Psi'(x)\end{pmatrix}.$$

The spectral theorem [33] ensures that the orthogonal transformation diagonalizing $\mathsf{V}(x)$ also diagonalizes any function of $\mathsf{V}(x)$, such as $\mathsf{P}(x)$.

Substitution of Eq. (3) into Eq. (2) gives the equation for the wavefunction in adiabatic representation [32];

$$\begin{aligned}&\begin{pmatrix}\psi_+(x)\\ \psi_-(x)\end{pmatrix}'\\ &= \begin{pmatrix}\mathrm{i}\mathsf{p}/\hbar - \mathsf{p}^{-1}\mathsf{p}'/2 & 0\\ 0 & -\mathrm{i}\mathsf{p}/\hbar - \mathsf{p}^{-1}\mathsf{p}'/2\end{pmatrix}\begin{pmatrix}\psi_+(x)\\ \psi_-(x)\end{pmatrix}\\ &\quad -\frac{1}{2}\begin{pmatrix}\mathsf{D} + \mathsf{p}^{-1}\mathsf{D}\mathsf{p} & \mathsf{D} - \mathsf{p}^{-1}\mathsf{D}\mathsf{p} - \mathsf{p}^{-1}\mathsf{p}'\\ \mathsf{D} - \mathsf{p}^{-1}\mathsf{D}\mathsf{p} - \mathsf{p}^{-1}\mathsf{p}' & \mathsf{D} + \mathsf{p}^{-1}\mathsf{D}\mathsf{p}\end{pmatrix}\\ &\quad \times \begin{pmatrix}\psi_+(x)\\ \psi_-(x)\end{pmatrix},\end{aligned} \tag{4}$$

where

$$\mathsf{D}(x) = \mathsf{Z}^{-1}(x)\,\mathsf{Z}'(x) = \mathsf{Z}^{T}(x)\,\mathsf{Z}'(x)$$

is the antisymmetric (and consequently off-diagonal) non-adiabatic transition matrix. Antisymmetry of $\mathsf{D}(x)$ follows from differentiation of $\mathsf{Z}^{\mathrm{T}}(x)\,\mathsf{Z}(x) = \mathsf{1}$. In Eq. (4), and elsewhere as required, the x dependencies in the matrices on the right are suppressed to make the equation more readable.

At this stage it is worth noting that the transformation to adiabatic representation is essential to the formulation of the shift equations iteration. In adiabatic representation, the left and right-going motions appear as separate components of the system state. In the case of a "seed" wave incoming from the left, the right-going component is specified on the left, while the left-going component is specified on the right—the latter is identically zero. These boundary conditions are not well suited to the more familiar Schrödinger representation of Eq. (2). While it is possible to formulate the shift equations iteration in terms of the adiabatic representation of Eq. (4), it is desirable to go a step further and introduce the n-level system WKB representation. In this representation, variation in the system state components arises entirely from the breakdown of adiabaticity. This circumstance is convenient for the purpose of demonstrating, via argument, the stability of the associated shift equations iteration—see Sect. 3.3. Construction of the WKB representation begins with consideration of the adiabatic approximation.

The adiabatic approximation (or the generalization of the WKB approximation to the n level system) is given by

neglecting the couplings between $\psi_+(x)$ and $\psi_-(x)$ in the above equation. The result is $\psi_\pm(x) \cong \varphi_\pm(x)$, where $\varphi_\pm(x)$ is the solution to the separable equations,

$$\begin{aligned}\varphi'_\pm(x) &= \left[\pm \mathrm{i}\mathsf{p}(x)/\hbar - \mathsf{p}^{-1}(x)\,\mathsf{p}'(x)/2\right]\varphi_\pm(x);\\ \varphi_\pm(x) &= \left[\pm \mathbf{p}(x)\right]^{-1/2}\exp\left[\pm \mathrm{i}\mathbf{w}(x)/\hbar\right],\end{aligned} \tag{5}$$

where

$$\mathbf{w}(x) = \int_{x_0}^{x} \mathrm{d}x'\,\mathbf{p}\left(x'\right),$$

is the vector of adiabatic actions, defined with respect to some reference point, x_0. $\mathbf{p}(x)$ is the vector of adiabatic momenta—the diagonal elements of $\mathsf{p}(x)$. Note that the exponentiation and vector function multiplication appearing in Eq. (5) are understood here on a component-by-component basis. Also note the unconventional inclusion of the minus sign in the prefactor of $\varphi_-(x)$—equivalently,

$$\varphi_\pm(x) = -i\left[\mathbf{p}(x)\right]^{-1/2}\exp\left[-i\mathbf{w}(x)/\hbar\right].$$

This convention will be useful in a subsequent publication.

The WKB representation of the Schrödinger equation is obtained using WKB wavefunctions as basis functions. The Schrödinger equation becomes a first-order linear differential equation for the associated expansion coefficients which provide corrections to the WKB approximation, i.e., variation in the expansion coefficients.

Let

$$\begin{pmatrix}\psi_+(x)\\ \psi_-(x)\end{pmatrix} = \begin{pmatrix}\mathbf{c}_+(x)\,\varphi_+(x)\\ \mathbf{c}_-(x)\,\varphi_-(x)\end{pmatrix}, \tag{6}$$

where the vector multiplication is on a component-by-component basis. Substituting Eq. (6) into Eq. (4) gives

$$\begin{aligned}&\begin{pmatrix}\mathbf{c}'_+(x)\,\varphi_+(x)\\ \mathbf{c}'_-(x)\,\varphi_-(x)\end{pmatrix} + \begin{pmatrix}\mathbf{c}_+(x)\,\varphi'_+(x)\\ \mathbf{c}_-(x)\,\varphi'_-(x)\end{pmatrix}\\ &= \begin{pmatrix}\mathrm{i}\mathsf{p}/\hbar - \mathsf{p}^{-1}\mathsf{p}'/2 & 0\\ 0 & -\mathrm{i}\mathsf{p}/\hbar - \mathsf{p}^{-1}\mathsf{p}'/2\end{pmatrix}\begin{pmatrix}\mathbf{c}_+(x)\,\varphi_+(x)\\ \mathbf{c}_-(x)\,\varphi_-(x)\end{pmatrix}\\ &\quad -\frac{1}{2}\begin{pmatrix}\mathsf{D}+\mathsf{p}^{-1}\mathsf{D}\mathsf{p} & \mathsf{D}-\mathsf{p}^{-1}\mathsf{p}'-\mathsf{p}^{-1}\mathsf{D}\mathsf{p}\\ \mathsf{D}-\mathsf{p}^{-1}\mathsf{p}'-\mathsf{p}^{-1}\mathsf{D}\mathsf{p} & \mathsf{D}+\mathsf{p}^{-1}\mathsf{D}\mathsf{p}\end{pmatrix}\\ &\quad \times\begin{pmatrix}\mathbf{c}_+(x)\,\varphi_+(x)\\ \mathbf{c}_-(x)\,\varphi_-(x)\end{pmatrix}.\end{aligned} \tag{7}$$

Here, the second term on the left together with the first term on the right constitute the equations for the adiabatic approximation, weighted by multiplicative coefficients, $\mathbf{c}_\pm(x)$. These terms cancel leaving

$$\begin{aligned}&\begin{pmatrix}\varphi_+(x)\,\mathbf{c}'_+(x)\\ \varphi_-(x)\,\mathbf{c}'_-(x)\end{pmatrix}\\ &= -\frac{1}{2}\begin{pmatrix}\mathsf{D}+\mathsf{p}^{-1}\mathsf{D}\mathsf{p} & \mathsf{D}-\mathsf{p}^{-1}\mathsf{p}'-\mathsf{p}^{-1}\mathsf{D}\mathsf{p}\\ \mathsf{D}-\mathsf{p}^{-1}\mathsf{p}'-\mathsf{p}^{-1}\mathsf{D}\mathsf{p} & \mathsf{D}+\mathsf{p}^{-1}\mathsf{D}\mathsf{p}\end{pmatrix}\\ &\quad\times\begin{pmatrix}\varphi_+(x)\,\mathbf{c}_+(x)\\ \varphi_-(x)\,\mathbf{c}_-(x)\end{pmatrix}.\end{aligned} \tag{8}$$

In this last line, we re-express component-by-component vector multiplication as the equivalent diagonal matrix vector multiplication, where the diagonal matrix consists of the elements of one of the vectors. Specifically, $\mathbf{c}_\pm(x)\,\varphi_\pm(x) = \varphi_\pm(x)\,\mathbf{c}_\pm(x)$, where $\varphi_\pm(x)$ is the diagonal matrix constructed from the components of $\varphi_\pm(x)$. We now have

$$\begin{pmatrix}\mathbf{c}_+(x)\\ \mathbf{c}_-(x)\end{pmatrix}' = -\frac{1}{2}\begin{pmatrix}\varphi_+^{-1}\left[\mathsf{D}+\mathsf{p}^{-1}\mathsf{D}\mathsf{p}\right]\varphi_+ & \varphi_+^{-1}\left[\mathsf{D}-\mathsf{p}^{-1}\mathsf{p}'-\mathsf{p}^{-1}\mathsf{D}\mathsf{p}\right]\varphi_-\\ \varphi_-^{-1}\left[\mathsf{D}-\mathsf{p}^{-1}\mathsf{p}'-\mathsf{p}^{-1}\mathsf{D}\mathsf{p}\right]\varphi_+ & \varphi_-^{-1}\left[\mathsf{D}+\mathsf{p}^{-1}\mathsf{D}\mathsf{p}\right]\varphi_-\end{pmatrix}\times\begin{pmatrix}\mathbf{c}_+(x)\\ \mathbf{c}_-(x)\end{pmatrix}, \tag{9}$$

or more compactly,

$$\mathbf{c}'(x) = \mathsf{A}(x)\,\mathbf{c}(x). \tag{10}$$

The components of the strictly off-diagonal transition matrix, $\mathsf{A}(x)$, are given by

$$\begin{aligned}&A_{j'+,j+}(x)\\ &= -\frac{1}{2}\exp\left(\mathrm{i}\left[w_j(x) - w_{j'}(x)\right]/\hbar\right)\\ &\quad\times\left[\left(\frac{p_{j'}(x)}{p_j(x)}\right)^{1/2} + \left(\frac{p_j(x)}{p_{j'}(x)}\right)^{1/2}\right]D_{j',j}(x)\end{aligned} \tag{11}$$

and

$$\begin{aligned}&A_{j'-,j+}(x)\\ &= -\frac{1}{2}\exp\left(\mathrm{i}\left[w_j(x) + w_{j'}(x)\right]/\hbar\right)\\ &\quad\times\left[\left(\frac{-p_{j'}(x)}{p_j(x)}\right)^{1/2} - \left(\frac{p_j(x)}{-p_{j'}(x)}\right)^{1/2}\right]D_{j',j}(x)\end{aligned} \tag{12}$$

for level indices j and $j' \neq j$, and

$$A_{j-,j+}(x) = \frac{1}{2}\exp\left(2\mathrm{i}w_j(x)/\hbar\right)p_j^{-1}(x)\,\frac{\mathrm{d}}{\mathrm{d}x}p_j(x), \tag{13}$$

for $j' = j$. $D_{j',j}(x)$ is given by

$$\begin{aligned}D_{j',j}(x) &= \sum_{j''} Z^{-1}_{j',j''}(x)\,\frac{\mathrm{d}}{\mathrm{d}x}Z_{j'',j}(x)\\ &= \sum_{j''} Z_{j'',j'}(x)\,\frac{\mathrm{d}}{\mathrm{d}x}Z_{j'',j}(x).\end{aligned}$$

If the variations in the eigenvectors of $\mathsf{V}(x)$, the adiabatic levels, are expanded in terms of the eigenvectors themselves, the

resulting expansion coefficients are provided by the columns of $\mathsf{D}(x)$. The absence of diagonal elements is a consequence of normalization of the eigenvectors. In the case of unnormalized eigenvectors, diagonal elements in $\mathsf{D}(x)$ would appear, accounting for variation in the eigenvector norms.

3 The shift equations iteration method

Numerical solution of the Schrödinger equation for an n-level system appears to be relatively straightforward on the surface. For example, there are many methods available for local solution of the coupled differential equations in first- or second-order form. It is then simply a matter of satisfying the appropriate boundary conditions. For example, one can express the state at one boundary via propagation of the state at the other boundary. The resulting equation is then rearranged, see below, so that the specified portion of the boundary states (the boundary conditions) are isolated on one side of the equation, while the unknown portions of these states appear on the other side. The trouble with this approach is that when there are closed channels, there are exponentially growing and decaying solutions. The former dominate states propagated over any significant distance. The propagator from one boundary to the other becomes highly skewed, reflecting the collapse of propagating states towards the direction of maximum exponential growth. The system of equations arising when one imposes the boundary conditions is correspondingly ill conditioned. In any case, the presence of exponentially large terms in the computation leads to significant rounding errors.

Here, we develop an integration approach which addresses the exponential instability arising when there are closed channels. We have found that it is generally not possible to impose boundary conditions directly in terms of integration from one asymptotic region to another, i.e., except via a log-derivative approach. However, it is possible to match boundary conditions over smaller intervals. By expressing the matching of global boundary conditions in terms of the simultaneous matching of boundary conditions across a sequence of smaller intervals, the matrix ill-conditioning arising from the exponential instability is circumvented. Specifically, a sequence of points is considered, $x_0 = x_{\text{left}}, x_1, \ldots, x_N = x_{\text{right}}$, such that x_{left} and x_{right} are in the asymptotic regions on opposite sides of the interaction region. This formulation is suited to a Cartesian variable, x, and a set of potentials which admit transmission and reflection processes in the presence of closed channels, i.e., not just a radial coordinate for which only reflection processes are possible. Such systems are more demanding because integration both into and out-of a region with closed channels cannot be avoided [6]. In the case of a radial coordinate, all channels are closed on the left and the incoming seed wave must be incoming on the right. Here, we consider an incoming seed from the left. Thus, if one wished to consider a radial coordinate, the method described below would follow with right and left interchanged.

The idea is to simultaneously map x_j to x_{j+1}, for $j = 0, \ldots, N-1$. With this approach, the Schrödinger equation is integrated only between neighboring points—there is no global integration across the entire interval for which the mapping is highly skewed. However, the system state is required at many points simultaneously. The system of equations resulting when boundary conditions are imposed is of order $2nN$, as opposed to the order $2n$ obtained if boundary conditions are imposed by mapping across the entire interval. It would seem, e.g., if we used a general system of equations solver—that the resulting algorithm would have $\mathrm{O}\left(n^3N^3\right)$ operations. As such, the advantage of this small interval integration method is apparently lost—note that simply integrating across the interval has many fewer operations, $\mathrm{O}\left(n^3N\right)$. However, because the system of equations is banded, the method can be formulated to be linear in the number of steps, N, across the interval, and thus have no scaling disadvantage, i.e., SEI is also an $\mathrm{O}\left(n^3N\right)$ method.

3.1 Matching boundary conditions via shift equations

Consider the mapping from x_j to x_{j+1} with the system state expressed in WKB representation,

$$\begin{pmatrix} \mathbf{c}_+^{(j+1)} \\ \mathbf{c}_-^{(j+1)} \end{pmatrix} = \begin{pmatrix} \mathsf{F}_{++}^{(j+1)} & \mathsf{F}_{+-}^{(j+1)} \\ \mathsf{F}_{-+}^{(j+1)} & \mathsf{F}_{--}^{(j+1)} \end{pmatrix} \begin{pmatrix} \mathbf{c}_+^{(j)} \\ \mathbf{c}_-^{(j)} \end{pmatrix}.$$

As written, this is the solution to Eq. (10) determined by some numerical integration from x_j to x_{j+1} (see below). However, because of the appearance of large exponential factors in the transition matrix elements connecting *from* closed channels (i.e., $\mathsf{F}_{\cdot,\text{closed}}^{(j+1)}$), it is better to work with Eq. (10) with all exponential factors in transition elements left out. This corresponds to a *local* WKB representation with the exponential behavior of the adiabatic solutions incorporated into the expansion coefficients. In this case, the basis functions consist only of the pre-exponential reciprocal square root momentum factors. In addition to eliminating unnecessary exponentially large transition elements, this alternate representation removes complications surrounding the choice of the reference point, x_0—specifically, it is always the current point x. We adopt local WKB representation henceforth with no change in notation. With this convention, the coefficients $\mathbf{c}_\pm(x)$ vary according to the exponential factors of the WKB functions, in the adiabatic limit, i.e., as opposed to being constant in this limit.

The set of all x_j to x_{j+1} maps, for $j = 0$ to $N-1$, can be combined into a single larger matrix equation which we term the shift equations,

$$\begin{pmatrix} \mathbf{c}_+^{(1)} \\ \mathbf{c}_-^{(1)} \\ \mathbf{c}_+^{(2)} \\ \mathbf{c}_-^{(2)} \\ \vdots \\ \mathbf{c}_+^{(N)} \\ \mathbf{c}_-^{(N)} \end{pmatrix} - \begin{pmatrix} \mathsf{F}_{++}^{(1)} & \mathsf{F}_{+-}^{(1)} & & & & & \\ \mathsf{F}_{-+}^{(1)} & \mathsf{F}_{--}^{(1)} & & & & & \\ & & \mathsf{F}_{++}^{(2)} & \mathsf{F}_{+-}^{(2)} & & & \\ & & \mathsf{F}_{-+}^{(2)} & \mathsf{F}_{--}^{(2)} & & & \\ & & & & \ddots & & \\ & & & & & \mathsf{F}_{++}^{(N)} & \mathsf{F}_{+-}^{(N)} \\ & & & & & \mathsf{F}_{-+}^{(N)} & \mathsf{F}_{--}^{(N)} \end{pmatrix} \times \begin{pmatrix} \mathbf{c}_+^{(0)} \\ \mathbf{c}_-^{(0)} \\ \mathbf{c}_+^{(1)} \\ \mathbf{c}_-^{(1)} \\ \vdots \\ \mathbf{c}_+^{(N-1)} \\ \mathbf{c}_-^{(N-1)} \end{pmatrix} = 0. \tag{14}$$

Here and below, we adopt the convention of making explicit only the non-zero portions of matrices (unless it is convenient to do otherwise). Thus, the unspecified portions of the above matrix consist only of zero elements.

At the boundaries, the system states are partially specified. For example, $\mathbf{c}_+^{(0)}$ is the incoming portion of the state on the left. Typically, $\mathbf{c}_+^{(0)}$ is a unit vector with component 1 associated with one of the open channels on the left. The other specified boundary condition is $\mathbf{c}_-^{(N)} = \mathbf{0}$, which corresponds to no incoming, or exponentially growing, components on the right. The components, $\mathbf{c}_-^{(0)}$ and $\mathbf{c}_+^{(N)}$, are unknowns to be determined by connecting the boundary conditions via the shift equations. In the case of open channel components, they consist of the reflection and transmission coefficients, respectively. Note that the case of a radial coordinate is also treated—with the understanding that left and right are interchanged (+ and −, i.e., left and right-going motions, would also be interchanged). In the case of a radial coordinate, r, all channels are closed at r_N, the smallest r value. The unknown coefficients there, $\mathbf{c}_-^{(N)}$, are exponentially small—the minus coefficients in local WKB representation decay exponentially to the left.

The key to the shift equations approach is to recast Eq. (14) such that the known parts of the boundary conditions are on one side of the equations, while the unknown parts are on the other side. To this end, we note that the first term on the left of Eq. (14) can be expressed in the form

$$\begin{pmatrix} \mathbf{c}_+^{(1)} \\ \mathbf{c}_-^{(1)} \\ \mathbf{c}_+^{(2)} \\ \mathbf{c}_-^{(2)} \\ \vdots \\ \mathbf{c}_+^{(N)} \\ \mathbf{c}_-^{(N)} \end{pmatrix} = \begin{pmatrix} \mathbf{0} \\ \mathbf{0} \\ \mathbf{0} \\ \mathbf{0} \\ \vdots \\ \mathbf{c}_+^{(N)} \\ \mathbf{0} \end{pmatrix} + \begin{pmatrix} 0 & 1 & 0 & & & \\ 0 & 0 & 1 & & & \\ \vdots & & & \ddots & & \\ \vdots & & & & 1 & 0 \\ & & & & 0 & 1 \\ 0 & \cdots & \cdots & & 0 & 0 \\ 0 & & & & 0 & 0 \end{pmatrix} \begin{pmatrix} \mathbf{c}_-^{(0)} \\ \mathbf{c}_+^{(1)} \\ \mathbf{c}_-^{(1)} \\ \vdots \\ \mathbf{c}_+^{(N-1)} \\ \mathbf{c}_-^{(N-1)} \end{pmatrix}. \tag{15}$$

Here, an extra component, $\mathbf{c}_-^{(0)}$, is added to the top of the vector on the right of Eq. (15). This is the unknown part of the state at the left boundary. The goal is to replace the two inequivalent vectors that appear in Eq. (14) by a single vector consisting only of the unknown components of the system state across the interval.

Looking at the second term in Eq. (14), we see that the first block-column of the matrix multiplies only the specified component, $\mathbf{c}_+^{(0)}$. Consequently, it can be stripped off and moved to the right side. At the same time, noting that $\mathbf{c}_+^{(N)}$ is an unknown, we append it to the bottom of the vector in the second term in Eq. (14) and augment the multiplying matrix with a zero column—with no net effect. Equation (14) now takes the form,

$$\begin{pmatrix} -\mathsf{F}_{+-}^{(1)} & 1 & 0 & & & & & 0 \\ -\mathsf{F}_{--}^{(1)} & 0 & 1 & & & & & 0 \\ & -\mathsf{F}_{++}^{(2)} & -\mathsf{F}_{+-}^{(2)} & \ddots & & & & 0 \\ & -\mathsf{F}_{-+}^{(2)} & -\mathsf{F}_{--}^{(2)} & & & & & 0 \\ & & & \ddots & & 1 & 0 & 0 \\ & & & & & 0 & 1 & 0 \\ & & & & & -\mathsf{F}_{++}^{(N)} & -\mathsf{F}_{+-}^{(N)} & 0 \\ & & & & & -\mathsf{F}_{-+}^{(N)} & -\mathsf{F}_{--}^{(N)} & 0 \end{pmatrix} \begin{pmatrix} \mathbf{c}_-^{(0)} \\ \mathbf{c}_+^{(1)} \\ \mathbf{c}_-^{(1)} \\ \vdots \\ \mathbf{c}_+^{(N-1)} \\ \mathbf{c}_-^{(N-1)} \\ \mathbf{c}_+^{(N)} \end{pmatrix} + \begin{pmatrix} \mathbf{0} \\ \mathbf{0} \\ \mathbf{0} \\ \mathbf{0} \\ \vdots \\ \mathbf{c}_+^{(N)} \\ \mathbf{0} \end{pmatrix} = \begin{pmatrix} \mathsf{F}_{++}^{(1)} \mathbf{c}_+^{(0)} \\ \mathsf{F}_{-+}^{(1)} \mathbf{c}_+^{(0)} \\ \mathbf{0} \\ \mathbf{0} \\ \vdots \\ \mathbf{0} \\ \mathbf{0} \end{pmatrix}$$

or

$$\begin{pmatrix} -\mathsf{F}_{+-}^{(1)} & 1 & 0 & & & & \\ -\mathsf{F}_{--}^{(1)} & 0 & 1 & & & & \\ & -\mathsf{F}_{++}^{(2)} & -\mathsf{F}_{+-}^{(2)} & \ddots & & & \\ & -\mathsf{F}_{-+}^{(2)} & -\mathsf{F}_{--}^{(2)} & & & & \\ & & & \ddots & 1 & 0 & \\ & & & & 0 & 1 & \\ & & & & -\mathsf{F}_{++}^{(N)} & -\mathsf{F}_{+-}^{(N)} & 1 \\ & & & & -\mathsf{F}_{-+}^{(N)} & -\mathsf{F}_{--}^{(N)} & 0 \end{pmatrix} \begin{pmatrix} \mathbf{c}_-^{(0)} \\ \mathbf{c}_+^{(1)} \\ \mathbf{c}_-^{(1)} \\ \vdots \\ \mathbf{c}_+^{(N-1)} \\ \mathbf{c}_-^{(N-1)} \\ \mathbf{c}_+^{(N)} \end{pmatrix} = \begin{pmatrix} \mathsf{F}_{++}^{(1)} \mathbf{c}_+^{(0)} \\ \mathsf{F}_{-+}^{(1)} \mathbf{c}_+^{(0)} \\ \mathbf{0} \\ \mathbf{0} \\ \vdots \\ \mathbf{0} \\ \mathbf{0} \end{pmatrix}. \tag{16}$$

3.2 Solving the system of equations via LU decomposition

The above system of equations is block quadridiagonal, and as such can be solved in economical fashion with order O (N) operations. To achieve this scaling, we explicitly construct the LU factorization of the coefficient matrix, and successively solve the associated L and U systems of equations. Solving the system of equations explicitly (see Appendix) permits a recasting of the solution into a form which manifestly avoids the exponential instability of the straightforward solution. A stable numerical algorithm is developed which affords a graphical interpretation as a kind of evolution across the interval and back.

Applying LU decomposition to Eq. (16) yields an iteration in terms of the blocks of L and U and the solution of the outer system equations, in addition to the components of $\mathbf{c}$ on the grid. Some of these blocks are expressed as the inverse of vanishingly small matrices, e.g., the blocks of U and the minus components of the solution, $\mathbf{b}$, to the outer system of equations in asymptotic regions. Nevertheless, it is possible to eliminate all the ill-defined vectors and matrices from the iteration (see Appendix) and get the following shift-equations iteration (SEI) equations.

$$\begin{aligned}
&\mathsf{L}^{(j)}_{\pm+} = \mathsf{F}^{(j)}_{\pm+}, \quad j = 1, \ldots, N, \\
&\mathsf{L}^{(j)}_{\pm-} = \mathsf{F}^{(j)}_{\pm-} + \mathsf{F}^{(j)}_{\pm+}\mathsf{L}^{(j-1)}_{+-}\left(\mathsf{L}^{(j-1)}_{--}\right)^{-1}, \quad j = 1, \ldots, N.
\end{aligned} \tag{17}$$

These first two equations determine the blocks of the L matrix as effective propagators (L-propagators) between neighboring points. While the $+$ to $\pm$ mappings, $\mathsf{L}^{(j)}_{\pm+}$, are just the elementary propagators, $\mathsf{F}^{(j)}_{\pm+}$, the $-$ to $\pm$ mappings, $\mathsf{L}^{(j)}_{\pm-}$, include an extra term which revisits the previous point, x_{j-2}. This L-propagation is depicted graphically in Fig. 1.

The solution to the outer system of equations—note that minus components are not needed—is generated concurrently with the blocks of L in the forward iteration;

$$\mathbf{b}^{(j)}_{+} = \left[\mathsf{F}^{(j)}_{++} - \mathsf{L}^{(j)}_{+-}\left(\mathsf{L}^{(j)}_{--}\right)^{-1}\mathsf{F}^{(j)}_{-+}\right]\mathbf{b}^{(j-1)}_{+}, \quad j = 1, \ldots, N. \tag{18}$$

The forward iteration ends at $j = N$ with

$$\mathbf{b}^{(N)}_{+} = \mathbf{c}^{(N)}_{+} = \mathbf{T},$$

the transmission coefficient. It is followed by an iteration back to $j = 1$,

$$\begin{aligned}
&\mathbf{c}^{(j)}_{+} = \mathbf{b}^{(j)}_{+} + \mathsf{L}^{(j)}_{+-}\left(\mathsf{L}^{(j)}_{--}\right)^{-1}\mathbf{c}^{(j)}_{-}, \quad j = N, \ldots, 1, \\
&\mathbf{c}^{(j-1)}_{-} = \left(\mathsf{L}^{(j)}_{--}\right)^{-1}\left[\mathbf{c}^{(j)}_{-} - \mathsf{F}^{(j)}_{-+}\mathbf{b}^{(j-1)}_{+}\right], \quad j = N, \ldots, 1.
\end{aligned} \tag{19}$$

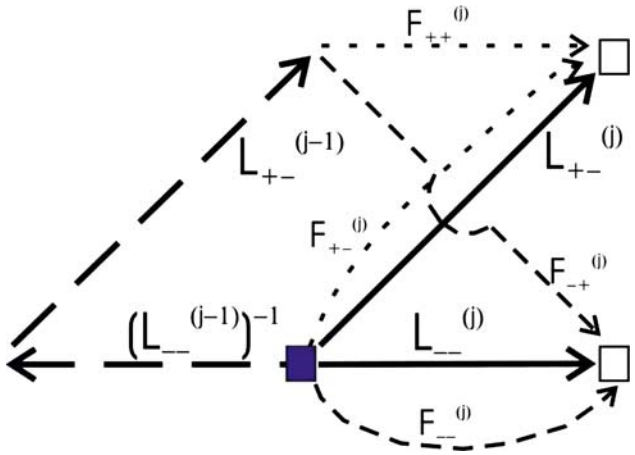

Fig. 1 Visualization of the construction of the $\mathsf{L}^{(j)}_{\pm-}$ mappings according to Eqs. (26) and (27). The $\mathsf{L}^{(j)}_{\pm-}$ are depicted as *solid arrows* connecting—components at x_{j-1} (the *solid square*) to $+$ and—components at x_j —the *top* and *bottom open squares*, respectively. $\mathsf{L}^{(j)}_{--}$ is constructed as the sum of two terms: (1) the direct contribution, $\mathsf{F}^{(j)}_{--}$, represented by the *bottom medium-dashed curve*, and (2) $\left(\mathsf{L}^{(j-1)}_{--}\right)^{-1}$, which maps backwards to x_{j-2}, followed by $\mathsf{L}^{(j-1)}_{+-}$ mapping the resulting—components at x_{j-2} to $+$ components at x_{j-1}, and $\mathsf{F}^{(j)}_{-+}$ which takes the $+$ components at x_{j-1} to—components at x_j. The former two mappings are depicted by *long-dashed arrows*, while the latter mapping appears as a *medium-dashed arrow*. $\mathsf{L}^{(j)}_{+-}$ is similarly constructed. The direct contribution is $\mathsf{F}^{(j)}_{+-}$, the *middle short-dashed arrow*. The indirect contribution consists of the same first two mappings in the indirect contribution to $\mathsf{L}^{(j)}_{--}$, namely $\left(\mathsf{L}^{(j-1)}_{--}\right)^{-1}$ and $\mathsf{L}^{(j-1)}_{+-}$, followed by $\mathsf{F}^{(j)}_{++}$ (the *top short-dashed curve*) which maps to $+$ components at x_j. $\mathsf{L}^{(j-1)}_{\pm-}$ are determined in the previous step of the shift equations iteration which is initialized by $\mathsf{L}^{(1)}_{\pm-} = \mathsf{F}^{(1)}_{\pm-}$, i.e., there are no long-dashed arrow contributions in the first step

The minus components, $\mathbf{c}^{(j-1)}_{-}$, of the energy eigenfunction are given by successive L-propagations back across the interval, subtracting out the $-$ to $+$ propagation of $\mathbf{b}^{(j-1)}_{+}$ from x_{j-1} to x_j at each point. Figure 2 represents this propagation, and that of the plus components, graphically. The back propagation ends at $j = 1$ with

$$\mathbf{c}^{(0)}_{-} = \mathbf{R},$$

the reflection coefficient. The shift equations iteration result in a numerical method upon adoption of a suitable integrator to determine the blocks of the F matrix. First, however, we investigate the stability of SEI.

3.3 Stability of the shift equations iteration

In the case of $N = 1$, SEI reduces to (suppressing the superscript on the propagator matrix in the case of a single step)

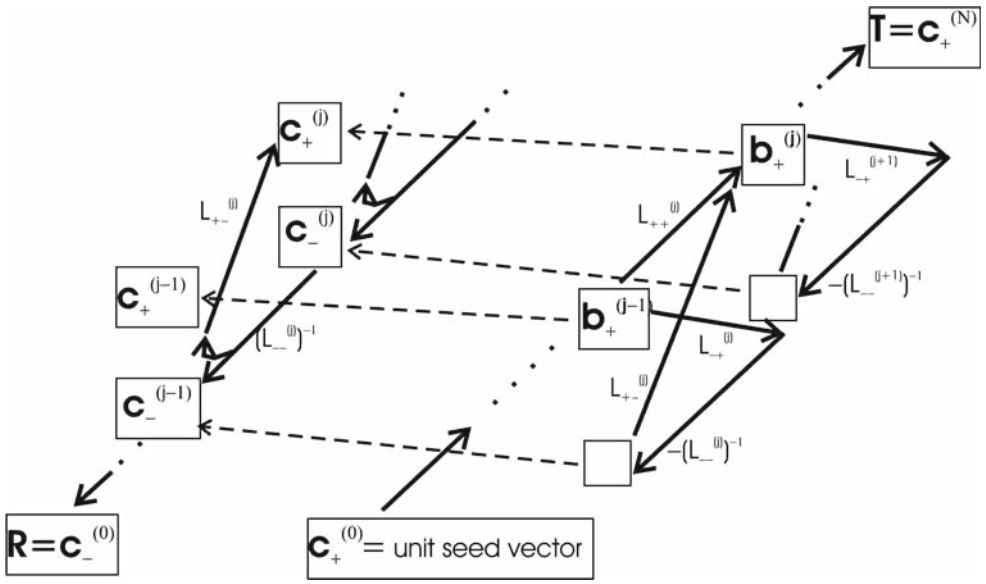

Fig. 2 Visualization of the construction of $\mathbf{b}_+^{(j)}$, $\mathbf{c}_+^{(j)}$ and $\mathbf{c}_-^{(j-1)}$ according to Eqs. (28), (29) and (30). $\mathsf{L}_{\pm\pm}^{(j)}$ mappings are depicted as *solid arrows* connecting n component system + or—states represented by boxes. Each state (except the initial seed state, $\mathbf{c}_+^{(0)}$, which is the unit vector in the seed channel) is a sum of contributions represented by arrows, labeled by the associated mapping, pointing to the box. *Dashed arrows* correspond to the identity mapping. The transmission and reflection coefficients, **T** and **R**, appear as end states on the right and left, respectively

$$\begin{pmatrix} \mathbf{c}_-^{(0)} \\ \mathbf{c}_+^{(1)} \end{pmatrix} = \begin{pmatrix} -\left(\mathsf{F}_{--}\right)^{-1}\mathsf{F}_{-+}\mathbf{c}_+^{(0)} \\ \left[\mathsf{F}_{++} - \mathsf{F}_{+-}\left(\mathsf{F}_{--}\right)^{-1}\mathsf{F}_{-+}\right]\mathbf{c}_+^{(0)} \end{pmatrix}. \tag{20}$$

This is just the result obtained by matching boundary conditions via propagation across the entire interval from $x_0 = x_{\text{left}}$ to $x_1 = x_{\text{right}}$. This formula is somewhat reminiscent of the Feschbach formula for the resolvent in terms of projections onto open and closed channel subspaces.[4] The matrix algebra is equivalent. As already discussed, the $N = 1$ formula is not useful if closed channels are present. The propagator, F, across the entire interval has very large (and small) eigenvalues whenever there are closed channels. For example, consider that in the WKB (i.e., adiabatic) approximation, the $\mathbf{c}_\pm$ consist of WKB exponential functions. Those associated with closed channels decay (+) or grow (−) from left to right across classically unallowed intervals. The largest such components are those associated with the highest energy level. While the WKB approximation may break down over large intervals (e.g., break down is assured across turning points), exponentially large eigenvalues of F remain. In any case, the large components have undesirable numerical consequences. First, the other components of the propagator are not accurately determined because of rounding error resulting from large component contributions. At each step in the integration of the propagator across the interval, the large components make contributions to the other components which eventually become impossible to accumulate accurately. The other problem associated with the large components is that exponential blow-up in closed channels is not shared by the solution which satisfies the boundary conditions. Consequently, the desired solution can arise from Eq. (20) only as a result of cancellation of the large terms, with significant associated rounding errors. Also, because of the exponential growth of closed channel components, the largest elements of F_{--} are exponentially larger than the other elements (also large in the case of other closed channels). Factor out the largest element of F, and the remaining elements are exponentially small—except those in the bottom row (i.e., those associated with the highest energy level). Thus, the columns of F_{--} are nearly proportional, i.e., it is nearly singular. These characteristics of the F matrix have been observed numerically for specific two-level systems, though the rounding errors described above pose the principal numerical difficulty.

The shift equations approach, derived above, avoids the pitfalls of Eq. (20) by working with the propagator across small intervals. Clearly the propagator can be computed accurately across small intervals. What remains is to verify that numerical instability does not return upon traversing the full interval via a succession of small intervals. As a point of reference, consider the accumulation of F via simple matrix multiplication of small interval propagators. In particular, consider the propagator for two successive small intervals, the jth and $j + 1$th,

[4] Equation (20) is a variation on the Feschbach formula. See Refs. [34, 35].

$$\begin{pmatrix} \mathsf{F}_{++}^{(j+1)}\mathsf{F}_{++}^{(j)} + \mathsf{F}_{+-}^{(j+1)}\mathsf{F}_{-+}^{(j)} & \mathsf{F}_{++}^{(j+1)}\mathsf{F}_{+-}^{(j)} + \mathsf{F}_{+-}^{(j+1)}\mathsf{F}_{--}^{(j)} \\ \mathsf{F}_{-+}^{(j+1)}\mathsf{F}_{++}^{(j)} + \mathsf{F}_{--}^{(j+1)}\mathsf{F}_{-+}^{(j)} & \mathsf{F}_{-+}^{(j+1)}\mathsf{F}_{+-}^{(j)} + \mathsf{F}_{--}^{(j+1)}\mathsf{F}_{--}^{(j)} \end{pmatrix}.$$

The blocks that map to $-$ components, i.e., $\mathsf{F}_{-\pm}^{(j')}$, apply expansion factors (i.e., factors greater than unity) to closed-channel components. Contributions to the x_{j-1} to x_{j+1} mapping shown above consisting of products of such blocks—namely $\mathsf{F}_{--}^{(j+1)}\mathsf{F}_{-+}^{(j)}$ and $\mathsf{F}_{--}^{(j+1)}\mathsf{F}_{--}^{(j)}$—multiply these expansion factors, and exponential growth arises upon accumulation of the propagator over many small intervals. In contrast, iterating Eqs. (27) and (28) in the forward direction, and Eq. (30) in the reverse direction does not result in exponential growing states. To see this, first note that since $\mathbf{c}_+^{(j)}$ does not appear on the right side of the final form of the iteration equations, it is not necessary to assess Eq. (29) for potential exponential growth. Consider now the iteration in the forward direction. The $\mathsf{L}_{\pm-}^{(j)}$ blocks have the same sort of expansion and contraction factors, of the same order, as the $\mathsf{F}_{\pm-}^{(j)}$ blocks. This is proved by induction, as follows. For $j = 1$, $\mathsf{L}_{\pm-}^{(1)} = \mathsf{F}_{\pm-}^{(1)}$. Assume the statement for the $j-1$th blocks. Equation (27) assures the result for the jth blocks—the second term on the right generally contributes smaller elements than the first, as only $\mathsf{L}_{--}^{(j-1)}$ contains expansion factors and it appears only in its inverse form.

Turning to Eq. (28), we see that $\mathbf{b}_+^{(j)}$ does not pick up expansion factors relative to $\mathbf{b}_+^{(j-1)}$. The expansion factors introduced by $\mathsf{F}_{-+}^{(j)}$ are countered by contraction factors associated with $\left(\mathsf{L}_{--}^{(j)}\right)^{-1}$. Therefore, forward iteration is stable, as long as the intervals are sufficiently small to justify the application of the WKB (adiabatic) approximation for integration from x_j to x_{j+1}. In practice, the intervals can be much larger. The above stability argument requires only that expansion factors are confined to $\mathsf{F}_{-\pm}^{(j)}$. Leakage of expansion factors into the other two blocks only occurs well past the point the WKB approximation begins to break down.

The equations are better behaved numerically if, instead of propagating $\mathbf{c}_\pm(x)$, we propagate $\psi_\pm(x)$. The only difference between these choices is a square root momentum factor—recall that $\mathbf{c}_\pm(x)$ is the local WKB representation (i.e., the origin of the action integrals in the WKB basis functions is x, and the basis functions reduce to prefactors). The above equations hold with $\mathbf{c}_\pm^{(j)}$ replaced by $\psi_\pm^{(j)}$, if we let $\mathsf{F}^{(j)}$ denote the propagator in $\psi_\pm$ representation. The argument guaranteeing convergence of the iteration, for sufficiently small intervals, still holds. The square root momentum factors associated with transformation to $\psi_\pm$ representation do not contribute to exponential instability. However, they do cause numerical problems in the neighborhood of turning points, if computations are carried out in $\mathbf{c}_\pm$ representation. Numerical methods based on truncated Taylor expansion of the system state are inaccurate in the neighborhood of turning points if $\mathbf{c}_\pm(x)$ represents the system state. Since turning points are not branch points of $\psi_\pm(x)$, there is no such numerical problem in adiabatic representation. Crossing points are branch points of $\psi_\pm(x)$. But, they occur off the real axis and do not pose a problem in this article. Note that, while $\mathbf{c}_\pm^{(j)}$ computed directly from the shift equations iteration is not accurate in the neighborhood of turning points, we have found that it is nevertheless accurate in the asymptotic regions. In particular, reflection and transmission coefficients are computed accurately in $\mathbf{c}_\pm$ or $\psi_\pm$ representation.

3.4 A symplectic log-derivative propagator

The exponential instability addressed via the shift equations is also addressed by log-derivative methods [7–10]. In fact, log-derivative methods provide the current standard of stability and efficiency among integration-type methods, i.e., solutions of close coupled equations. The symplectic log-derivative method of Manolopoulos and Gray [25] based on the McLachlan Atela [26] six-step fifth order symplectic integrator (MA5), is a very efficient example of such methods. For this reason, and because it is easily implemented, it is chosen as our means of constructing the propagator matrix at each step of the shift equations iteration. To use this approach, the state expressed in $\psi_\pm$ representation is transformed to $\Psi - \mathbf{Y}$ representation. Thus, we effectively return to Eq. (2) in the numerics. Note, however, that SEI is still implemented in adiabatic representation—the propagator matrix determined in $\Psi - \mathbf{Y}$ representation is transformed back to $\psi_\pm$ representation at each step. The reason for doing this is to access the numerical efficiency of the log-derivative approach which is formulated in terms of Ψ and Ψ'. It is possible to work entirely within $\psi_\pm$ representation, using SEI, and we have done this. In particular, we have used direct Runga–Kutta integration of Eq. (4). However, the most efficient approach was the log-derivative approach we present here, see Table 2 for a comparison of methods. Each block of the propagator matrix results from propagation of n unit vectors in $\psi_\pm$ representation, e.g., $\mathsf{F}_{\pm+}^{(j)}$ results from propagation of the $n \times n$ identity matrix, $\psi_+\left(x_{j-1}\right)$, at x_{j-1}, to $\psi_\pm\left(x_j\right)$ at x_j. Transforming the former to $\Psi - \mathbf{Y}$ representation and propagating according to MA5 determines $\Psi_\pm^{(j)}$ and $\mathsf{Y}_\pm^{(j)} = \Psi_\pm'^{(j)}(\Psi_\pm^{(j)})^{-1}$. Two $n \times n$ wavefunction matrices, ψ_+ and ψ_-, are propagated in $\Psi - \mathbf{Y}$ representation via this symplectic log-derivative integrator. This is unlike usual implementations of log-derivative propagation wherein only one $n \times n$ wavefunction matrix is propagated. In the latter implementations, it is sufficient to propagate only n wavefunctions because the solutions excluded are either asymptotically divergent in closed channels or have components incoming from the right in open channels. To use log-derivative propagation within the shift equations

framework, two sets of n solutions are required because the starting point in the propagation, x_{j-1}, is mostly not asymptotic. The $\Psi - \mathbf{Y}$ blocks determined by log-derivative propagation are related to the blocks of the F matrix as follows:

$$\begin{pmatrix} \Psi_+^{(j)} & \Psi_-^{(j)} \\ \mathsf{Y}_+^{(j)} & \mathsf{Y}_-^{(j)} \end{pmatrix} = \begin{pmatrix} \mathsf{Z}_j \left[\mathsf{F}_{++}^{(j)} + \mathsf{F}_{-+}^{(j)} \right] & \mathsf{Z}_j \left[\mathsf{F}_{+-}^{(j)} + \mathsf{F}_{--}^{(j)} \right] \\ (\mathrm{i}\mathsf{P}_j/\hbar)\, \mathsf{Z}_j \left[\mathsf{F}_{++}^{(j)} - \mathsf{F}_{-+}^{(j)} \right] \left[\mathsf{F}_{++}^{(j)} + \mathsf{F}_{-+}^{(j)} \right]^{-1} (\mathsf{Z}_j)^{-1} & (\mathrm{i}\mathsf{P}_j/\hbar)\, \mathsf{Z}_j \left[\mathsf{F}_{+-}^{(j)} - \mathsf{F}_{--}^{(j)} \right] \left[\mathsf{F}_{+-}^{(j)} + \mathsf{F}_{--}^{(j)} \right]^{-1} (\mathsf{Z}_j)^{-1} \end{pmatrix}. \tag{21}$$

Inversion of Eq. (21) determines the blocks of the $\mathsf{F}^{(j)}$ matrix, used in the shift equations iteration, in terms of log-derivative propagation. Specifically,

$$\begin{pmatrix} \mathsf{F}_{++}^{(j)} & \mathsf{F}_{+-}^{(j)} \\ \mathsf{F}_{-+}^{(j)} & \mathsf{F}_{--}^{(j)} \end{pmatrix} = \begin{pmatrix} \mathsf{Z}_j^{-1}\mathsf{P}_j^{-1} \left[\mathsf{P}_j - \mathrm{i}\hbar \mathsf{Y}_+^{(j)} \right] \Psi_+^{(j)}/2 & \mathsf{Z}_j^{-1}\mathsf{P}_j^{-1} \left[\mathsf{P}_j - \mathrm{i}\hbar \mathsf{Y}_-^{(j)} \right] \Psi_-^{(j)}/2 \\ \mathsf{Z}_j^{-1}\mathsf{P}_j^{-1} \left[\mathsf{P}_j + \mathrm{i}\hbar \mathsf{Y}_+^{(j)} \right] \Psi_+^{(j)}/2 & \mathsf{Z}_j^{-1}\mathsf{P}_j^{-1} \left[\mathsf{P}_j + \mathrm{i}\hbar \mathsf{Y}_-^{(j)} \right] \Psi_-^{(j)}/2 \end{pmatrix}, \tag{22}$$

with $\Psi_\pm$ and $\mathsf{Y}_\pm$ propagated via the MA5 six-step symplectic integrator. In particular, the interval (x_{j-1}, x_j) is divided into $N_{\mathrm{MA5}}\delta x$-width subintervals, with propagation across such a subinterval executed in six substeps,

$$\begin{aligned} x_k &= x_{k-1} + \alpha_k \delta x \\ \Psi'(x_k) &= \Psi'(x_{k-1}) - \beta_k \mathsf{P}^2(x_{k-1})\, \Psi(x_{k-1})\, \delta x/\hbar^2 \\ \Psi(x_k) &= \Psi(x_{k-1}) + \alpha_k \Psi'(x_k)\, \delta x, \quad k = 1, \ldots, 6 \end{aligned} \tag{23}$$

Here, (x_{k-1}, x_k) is a subinterval of a δx-width subinterval. The six α_k and β_k coefficients, producing a $\mathrm{O}(\delta x^5)$ error with the smallest sixth-order contribution, were determined by McLachlan and Atela [26]. Values are given in Table 1.

Equations (23) are a discretization of Hamilton's equations for an effective harmonic oscillator system for which x serves as the time coordinate. The force constant for the effective harmonic oscillator is x dependent—specifically, $\mathsf{P}^2(x_{k-1})/\hbar^2$ [25]. The iteration is symplectic because each step corresponds to exact pure potential propagation—drop the kinetic energy of effective harmonic oscillator Hamiltonian and replace $\mathsf{P}^2(x)$ by the piece-wise constant approximation, $\mathsf{P}^2(x) = \mathsf{P}^2(x_{k-1})$ in each subinterval $(x_{k-1} < x < x_k)$—followed by exact pure kinetic (i.e., free particle) propagation—just drop the potential term. The x-dependent effective Hamiltonian is thus replaced by a discretely varying effective Hamiltonian with kinetic and potential portions alternately turned on and off across the interval. Equations (23) provide the exact evolution for the resulting Hamiltonian system, and as such conserve all the Poincaré integral invariants, i.e., they are symplectic.

Table 1 Coefficients for the McLachlan Atela six-step fifth order symplectic integrator (MA5) [26]

$\alpha_1 = 0.339\,839\,625\,839\,11$	$\beta_1 = 0.119\,390\,029\,287\,57$
$\alpha_2 = -0.088\,601\,336\,903\,027$	$\beta_2 = 0.698\,927\,370\,382\,48$
$\alpha_3 = 0.585\,8564\,768\,259\,6$	$\beta_3 = -0.171\,312\,358\,271\,60$
$\alpha_4 = -0.603\,039\,356\,536\,49$	$\beta_4 = 0.401\,269\,502\,251\,35$
$\alpha_5 = 0.323\,580\,796\,554\,70$	$\beta_5 = 0.010\,705\,081\,848\,236$
$\alpha_6 = 0.442\,363\,794\,219\,75$	$\beta_6 = -0.058\,979\,625\,498\,031$

Manolopoulos and Gray [25] convert Eqs. (23) to log-derivative form in response to the exponential divergence problem. They explain how the accuracy of the log-derivative equations,

$$\begin{aligned} \mathsf{X}(x_k) &= \mathsf{Y}(x_{k-1}) - \beta_k \mathsf{P}^2(x_{k-1})\, \delta x/\hbar^2 \\ \mathsf{Y}(x_k) &= \left[1 + \alpha_k \mathsf{X}(x_k)\, \delta x\right]^{-1} \mathsf{X}(x_k) \\ \Psi(x_k) &= \left[1 - \alpha_k \mathsf{Y}(x_k)\, \delta x\right]^{-1} \Psi(x_{k-1}), \end{aligned} \tag{24}$$

is governed solely by the convergence of the Taylor series for $\Psi(x)$ rather than those of $\mathsf{Y}(x)$, explaining why the poles of $\mathsf{Y}(x)$ do not cause numerical difficulties.

In Sect. 4, the SEI is implemented as described above for two 2 level systems. It is found to provide convergence characteristics comparable to the best log-derivative results seen in Ref. [6], i.e., besides from the overhead of integrating $2n$ wavefunctions rather than just n, and the implementation of the iteration equations (only once every $6N_{\mathrm{MA5}}$ implementations of Eqs. (24), however). The advantage of the shift equations approach is that it circumvents the exponential divergence problem with or without use of log-derivative propagation. In particular, it provides both reflection and transmission coefficients, and wavefunctions, directly without exponential divergence. This is important because log-derivative methods, in their usual formulation, do not generally provide transmission coefficients free of exponential divergence. Reference [6] describes how to extend log-derivative methods to get such transmission coefficients. However, it is not clear that exponential-divergence-free wavefunctions can be obtained with log-derivative methods.

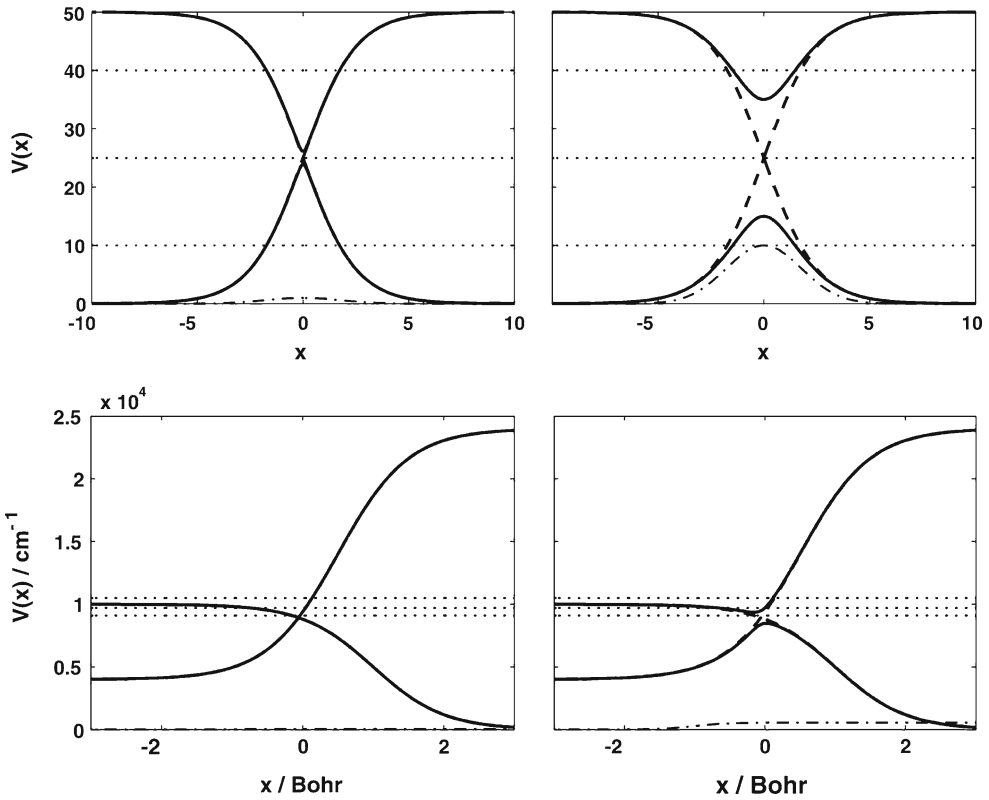

Fig. 3 Two-level model system potential energy curves. Adiabatic (*solid lines*) and diabatic (*dashed lines*) curves are shown. (Note that dashed diabatic curves are not visible in the tight avoided crossing models on the left.) The coupling between diabatic levels is shown as a *dot-dashed line*. *Dotted horizontal lines* indicate the energies investigated in the convergence study—see Fig. 7 and Tables 2 and 3—and some of the energies for which wavefunctions are plotted. The *upper panels* are two instances of the model in Ref. [36] designated as "potential A". The left of these shows a tight avoided crossing, while the right shows a loose avoided crossing due to a stronger Gaussian coupling. The lower panels are two examples of the model called "potential B", the left of which taken directly from Ref. [6]. The *bottom right panel* is the same as the left except for a larger coupling function which produces a looser avoided crossing

Generally, log-derivative methods are best suited to radial problems which do not have transmission channels. The shift equations iteration is well suited to two-sided problems with multiple open channels. Examples of such problems include quantum or molecular wires [18–20].

4 Numerical results

4.1 Two-level model systems

The SEI is tested on simple two-level systems from Refs. [6, 36]—all with particle mass, $m = 1$. They represent generic examples of avoided crossing in two-sided systems—non-adiabatic tunneling systems in the words of Zhu and Nakamura [27]. All the systems treated here are two-sided models with both reflection and transmission coefficients. Two-sided systems highlight a unique strength of the SEI, namely the elimination of exponential blow-up in transmission as well as reflection coefficients. All results shown were obtained via solution of the equations of Sect. 2.2 with F matrices provided by symplectic log-derivative integration between successive x_j.

The potential energies for the model systems considered below are shown in Fig. 3. The top two panels are from Ref. [36]. They are instances of what we term potential A, defined by

$$V_{11}(x) = V_0\,[1 + \tanh(x/\Delta x)],$$
$$V_{22}(x) = V_0\,[1 - \tanh(x/\Delta x)]$$

and,

$$V_{12}(x) = V_{21}(x) = C_0 \exp\left(-x^2/\Delta x^2\right),$$

with $V_0 = 25$, $\Delta x = 2.5$ and $C_0 = 1$ and 10 (top left and right panel, respectively). They represent tight and loose symmetric avoided crossings. The bottom left panel is a model studied in Ref. [6]. The bottom right panel is the same model, potential B, with the coupling between diabatic levels arbitrarily increased so that the bottom two panels provide examples of tight and loose asymmetric avoided

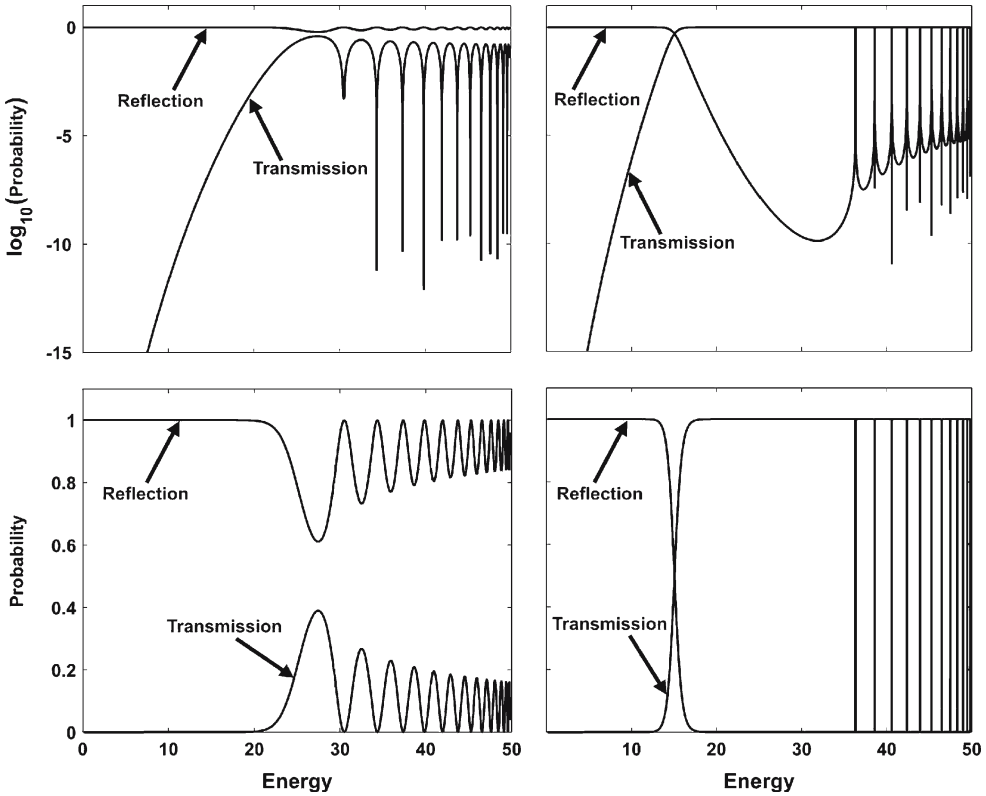

Fig. 4 Asymptotic transmission and reflection flux probabilities as a function of energy for an incoming seed of unit flux in the ground level. The *left panels* correspond to computations done on the upper-left panel potential A model of Fig. 3. The *right panels* correspond to computations for the upper-right panel potential A model of Fig. 3. The *upper panels* provide log-plots to make visible the very small reflection and transmission probabilities above and below the barrier, respectively

crossing, respectively. In this model, all the elements of $\mathsf{V}(x)$ are expressed in terms of tanh functions [6]. In the case of potential B, all computations presented below are for waves incoming in the lower channel on the right, as opposed to the left in the case of potential A. This convention is in accordance with the computations of Ref. [6], and with radial coordinate models. To use the SEI with this convention, left and right must be interchanged in Sect. 3.

Figures 4 and 5 show the reflection and transmission probabilities (only transmission probabilities are shown in Fig. 5) computed using SEI with the symplectic log-derivative integrator of Manolopoulos and Gray [25] for potentials A and B, respectively. The left panels correspond to the tight avoided crossing models, while the right panels correspond to loose avoided crossings. The top panels are log plots of the same data. They provide a clearer view of the sharp resonances of the $C_0 = 10$ (loose avoided crossing case) potential A model (right panels of Fig. 4). Note that it was necessary to refine the energy grid used in these plots, via bisection in the neighborhoods of resonances, in order to adequately resolve the sharp features in the reflection and transmission probabilities. Actually, the sharp negative resonance peaks seen in the log-plots of transmission probabilities are generally still not fully resolved, as shown here. With resonance energies fully resolved, transmission probability goes much lower—on a much finer energy scale—than shown here. For example, the fourth lowest energy resonance of the loose avoided crossing potential A system, resolved to double precision accuracy, produces a transmission probability of 10^{-21}. According to Nakamura (see Chapter 11 of [29]), transmission probability is exactly zero right at resonance. Figure 6 shows high-resolution potential A system reflection and transmission probabilities for C_0 varied from 10 to 1. The resonances observed shift upon varying C_0 in accordance with the corresponding shift in the energy eigenvalues of the upper channel well with coupling to the lower channel turned off. Otherwise, they broaden as C_0 decreases. But, even the broadest resonances seen in Fig. 6—i.e., those for potential A with $C_0 = 1$—show transmission probability spiking below the bottom of the graph indicating very near 100% reflectivity at resonance. In any case, the broadening in the tight avoided crossing case is such that high-resonant reflectivity is spread over the entire above-barrier energy range—with $C_0 = 1$ the reflectivity is greater than transmissivity at all energies below

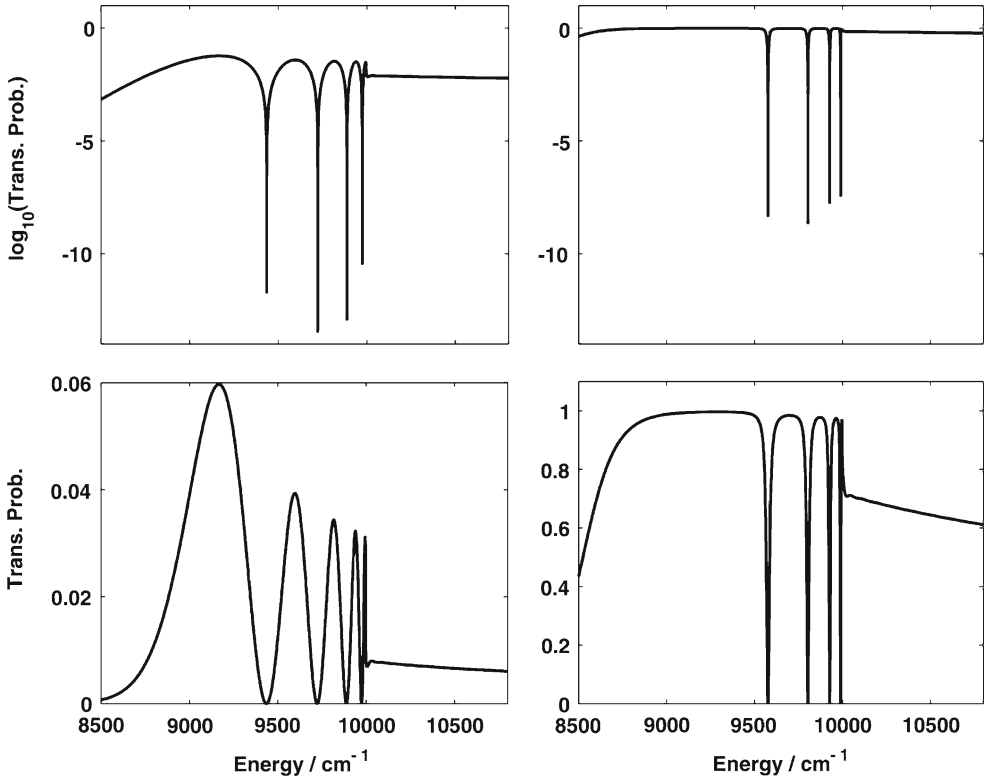

Fig. 5 As in Fig. 4 except the left panels are for the potential B model of the lower-left panel in Fig. 3, while the *right panels* correspond to the potential B model of the lower-right panel in Fig. 3

$E = 50$. This is consistent with the tight avoided crossing case being close to the diabatic limit. In the diabatic limit, the particle sees only the barrier on the right of the first diabatic potential. In terms of the adiabatic representation, the particle is excited to the upper level near $x = 0$, encounters the right wall of the upper level well, then returns to the lower level without encountering the left wall of the upper level well.

The loose avoided crossing case of potential B—the right panels of Fig. 5—shows four resonances as negative peaks in transmission probability, just as for potential A. These correspond to pseudo-bound states of the shallow but broad well in the upper channel. The tight avoided crossing case is the model used in Ref. [6]. The transmission probability shown in the left panels of Fig. 5 exactly reproduces Fig. 4 of Ref. [6]. So, the method works. But does it offer any advantage? To address this question, we first consider the results of some convergence studies analogous to those depicted in Fig. 5 of Ref. [6].

4.2 Convergence studies

Figure 7 shows the relative error in transmission probabilities for a series of potential B computations, with $N = 100$ and varying number of MA5 steps N_{MA5} used to compute requisite $\mathsf{F}^{(j)}$ matrices. We see that the transmission probability converges for fixed finite N. That is, SEI is exact if the integration for each step is converged. This is true for N down to about 20 for both potentials A and B. For smaller values of N, the associated $\mathsf{F}^{(j)}$ matrices diverge exponentially and cannot be computed sufficiently accurately to obtain transmission and reflection coefficients. In any case, the shift equations iteration is essentially exact. The error seen in the resulting transmission probabilities directly manifests the error in the $\mathsf{F}^{(j)}$ matrices. Additional computations (not shown here) indicate that that the error depends only on the product, $N_{\mathrm{total}} = N N_{\mathrm{MA5}}$ over a wide range of N and N_{MA5} values. Increasing the number of integration steps between grid points and increasing the number of grid points, N, produce the same accuracy.

Figure 7 can be compared directly with Fig. 5 of Ref. [6]. Consider the errors for $N_{\mathrm{total}} = 500$ total integration steps, given in Table 2. Results using SEI in combination with a number of different non-log-derivative integrators and with the log-derivative form of MA5 (ldMA5) described in Ref. [25] are included along with results estimated from Fig. 5 of Ref. [6]. The latter results are for log-derivative propagation in accord with Johnson [7] and Manolopoulos [10].

The errors in SEI with log-derivative MA5 (SEI-ldMA5) are seen to be smaller than those obtained in Ref. [6] using the method of Johnson [7], but not quite as small as those obtained with the reference half-interval method of Manolopoulos [10]. Because SEI-ldMA5 errors scale as

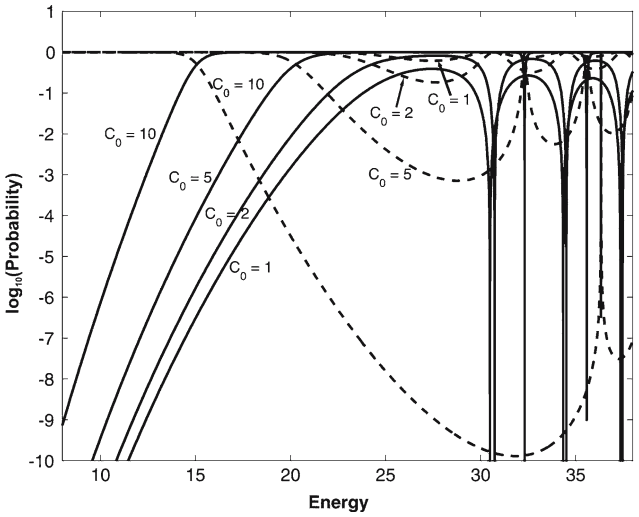

Fig. 6 Transmission (*solid lines*) and reflection (*dashed lines*) probabilities as functions of energy, for potential A, with varying coupling amplitude—$C_0 = 1$, 2, 5 and 10, as labeled

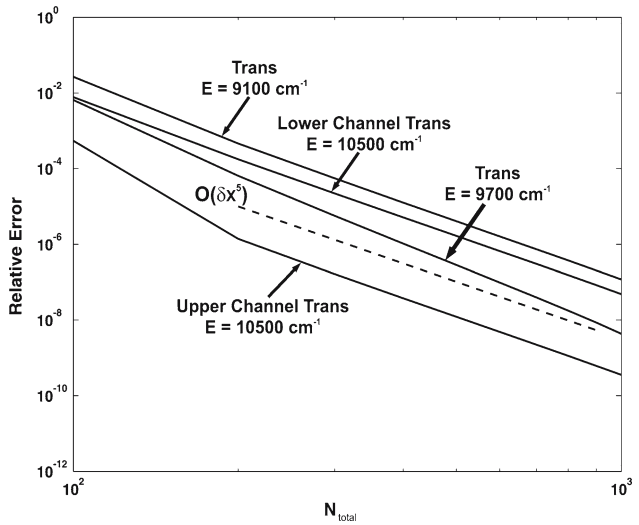

Fig. 7 Relative error in transmission probability as a function of the total number of integration steps computed, for potential B. $N = 100$ and $N_{\mathrm{MA5}} = 1$ to 10, giving $N_{\mathrm{total}} = 100$ to 1000. Curves are labeled according to energy and channel. Only the lower channel is open for the lower two energies. $\mathrm{O}(\delta x^5)$ (*dashed line*) is included to provide a reference slope (namely, −5)

$\mathrm{O}\left(N_{\mathrm{total}}^{-(5\text{ to }6)}\right)$, while Manolopoulos errors scale more like $\mathrm{O}\left(N_{\mathrm{total}}^{-(4\text{ to }4.4)}\right)$, SEI-ldMA5 is more accurate than the Manolopoulos algorithm for larger N_{total} (beginning around $N_{\mathrm{total}} = 1000$). This is not to say that SEI-ldMA5 is more efficient at these very high accuracies. We have made no attempt to count the total number of steps in the two computations. The point is only that SEI-ldMA5 performs comparably to a very efficient existing method. It is worth noting that computations of Ref. [25] show the log-derivative form of MA5 to outperform the original Johnson algorithm in a set of standard radial problems (Secrest–Johnson, Lester–Bernstein and Dunker–Gordon), in accordance with results shown here.

The non-log-derivative integrator formulations of SEI generally do not perform as well as SEI-ldMA5 in the case of potential B, see Table 2. However, for potential A, SEI with fifth order Runge–Kutta integration (RK5) or a fourth order adaptation of the leap-frog Verlet algorithm (V4) outperforms SEI-ldMA5 at the above-barrier energies, $E = 25$ and 40, see Table 3. It is noteworthy that these two or any other non-log-derivative algorithms cannot be used directly—i.e., outside of the shift equations iteration approach—to determine reflection and transmission probabilities. Non-log-derivative integrators diverge if used for intervals larger than about 1/20 of the range of x (i.e., $N \lesssim 20$). SEI allows these integrators to be useful by breaking the x range into intervals over which $\mathsf{F}^{(j)}$ can be computed accurately. In some cases, non-log-derivative integrators are as good as or better than SEI-ldMA5.

SEI-ldMA5 appears to perform quite well in most instances. In any case, it always converges. However, the real advantage of the shift equations approach is that it permits computation of both transmission and reflection coefficients with managed exponential growth (i.e., there is only exponential growth between successive grid points which the iteration does not accumulate). Log-derivative methods provide exponential-divergence-free reflection coefficients. But, in general, computation of the transmission coefficients requires the wavefunction across the interval. Reference [6] circumvents the exponential growth of wavefunctions by expressing the transmission coefficients in terms of the product of G matrices—$\mathsf{G}\left(x_{j-1}, x_j\right) = \Psi\left(x_{j-1}\right)\Psi^{-1}\left(x_j\right)$—accumulated on crossing the interval from the transmission region to the incoming region. The resulting product, $\mathsf{G}\left(x_{\mathrm{left}}, x_{\mathrm{right}}\right) = \Psi\left(x_{\mathrm{left}}\right)\Psi^{-1}\left(x_{\mathrm{right}}\right)$, is used to get the transmitted wave, $\Psi\left(x_{\mathrm{left}}\right)$, from the incoming plus reflected wave, $\Psi\left(x_{\mathrm{right}}\right)$. The latter wave is known in terms of the exponential-growth-free log-derivative. Because $\mathsf{G}\left(x_{\mathrm{left}}, x\right)$ is accumulated from left to right, ending at $x = x_{\mathrm{right}}$, exponential growth in $\Psi(x)$ manifests only as exponential decay. Consequently, the transmission coefficient computation of Ref. [6] is not subject to numerical overflow. Nevertheless, it is not clear how robust the method is in cases of multiple closed channels, since $\mathsf{G}\left(x_{\mathrm{left}}, x_{\mathrm{right}}\right)$ consists of a superposition of exponentially decaying terms in such cases. The potential B computations of Ref. [6] demonstrate the method works well for a two level system at energies with two open transmission channels, $E = 10{,}500\,\mathrm{cm}^{-1}$, and a closed channel on both the left and the right, $E = 9{,}100$ and $9{,}700\,\mathrm{cm}^{-1}$. We have verified these results using the Johnson algorithm of Ref. [6], and have shown the method to work for potential A and for a three- and a four-level system [24]. However, while the algorithm of Ref. [6] provided accurate transmission

Table 2 Convergence of potential B transmission probability computations

$-\log_{10}$ (trans. prob. err.[a])	Johnson[b]	Manolopoulos[b]	SEI-ldMA5	SEI-RK5[c]	SEI-RK4[d]	SEI-V4[e]
9,100 cm^{-1}	4.8	6.5	5.4	2.7	1.8	3.9
9,700 cm^{-1}	4.0	5.7	6.5	2.6	1.7	3.8
10,500 cm^{-1}, lower channel	6.5[f]	7.5[f]	5.8	2.4	1.5	3.6
10,500 cm^{-1}, upper channel	6.5	9.2[f]	7.9	2.6	1.7	3.6
− (best linear slope)						
9,100 cm^{-1}	4.4	4.3	5.1	5.0	5.0	4.2
9,700 cm^{-1}	4.2	4.0	6.0	5.0	5.0	4.3
10,500 cm^{-1}, lower channel	5.9	4.4	5.0	5.0	5.0	4.3
10,500 cm^{-1}, upper channel	3.8	4.3	5.1	5.0	5.0	4.2

Log_{10} of the error in transmission probability for 500 total integration steps, and the best linear slopes in the $\log_{10}$ (error) vs. log N_{total} plots
[a] Transmission probability is computed with $N_{\text{total}} = 500$ total integration steps
[b] These data are extracted from Fig. 5 of Ref. [6]
[c] Shift equations iteration with fifth order Runge–Kutta computation of the $\mathsf{F}^{(j)}$ matrices
[d] Shift equations iteration with fourth order Runge–Kutta
[e] Shift equations iteration with a fourth order adaptation of the leap-frog Verlet algorithm
[f] These numbers were obtained by extrapolating data shown in Fig. 5 of Ref. [6]

Table 3 Convergence of potential A transmission and reflection probability computations

$-\log_{10}$ (transit prob. error)	SEI-ldMA5	SEI-RK5	SEI-RK4	SEI-V4
10 (transmission)	11.0	4.3	3.5	5.9
25 (reflection)	3.9	6.7	4.0	5.3
40 (reflection)	4.0	5.0	2.9	5.1
− (best linear slope)				
10 (transmission)	5.7	5.0	5.1	4.3
25 (reflection)	5.7	6.0	4.0	3.9
40 (reflection)	6.2	6.0	4.0	3.5

Errors are for 1000 total integration steps. Otherwise, as in Table 2

coefficients, it did not provide accurate wavefunction components in the asymptotic region for closed channels. It is not yet clear whether the method can be adapted to provide accurate wavefunctions across the interval, including closed channel components. In any case SEI provides such results. The problem of exponential instability [2–4] is discussed in Ref. [6], but not in the context of computation of wavefunctions. They describe how numerical instability is addressed by an Airy function-based variation of the log-derivative method [5]. No convergence study for this latter algorithm is shown, however.

4.3 Wavefunctions

The shift equations iteration provides energy eigenfunctions at the x_j grid points. It is interesting to examine these wavefunctions. Figures 8, 9, 10 and 11 show wavefunctions for potential A with $C_0 = 10$, at $E = 10, 25, 36.3360539773469$ (the first resonance converged to double precision accuracy) and 42.3795273 (the fourth resonance), respectively. The first energy is in the tunneling regime. Here, we see the interference between the comparable (in amplitude) incoming and reflected waves, and the exponentially small tunneling amplitude. Figure 8 also shows the corresponding one-level system wavefunction (i.e., computed using only the lower adiabatic potential) and WKB right and left-going waves, for comparison. The one-level system wavefunction (the dot-dashed line in the top panel) is indistinguishable from the two-level system wavefunction, except for the small non-adiabatic-transition-related drop in the two-level system wavefunction beyond $x = 0$ (seen more clearly in the the inset). Similar plots are shown in Fig. 12 for potential A with $C_0 = 1$, at $E = 10$. The effect of the non-adiabatic transition is more pronounced in this case. In particular, the onset of this drop is clearly seen to occur at $x = 0$, the real part of the two complex conjugate crossing points. WKB wavefunctions, $\varphi_{\pm}(x)$, are also shown in the wavefunction figures—scaled to give the best fit (if possible) to the computed exact wavefunctions. Note the tiny divergent portions of the WKB wavefunctions at the turning points in the top panel of Fig. 8. In the tunneling regime, the lower channel (top panel) wavefunction is modeled by $\varphi_+(x) + \varphi_-(x)$, up to the first turning point (note that $|\varphi_+(x)|$ and $|\varphi_-(x)|$ match exactly to the left of the left turning point), and $\varphi_+(x)$ beyond (i.e., to the right). For $E = 25$ (Fig. 9), the lower channel (upper panel) wavefunction is modeled perfectly by $\varphi_+(x)$; i.e., it is a simple right-going wave across the interval with a small enhancement in the interaction region where the wave slows down due to the potential barrier. This is typical of all above-barrier wavefunctions except those near resonance

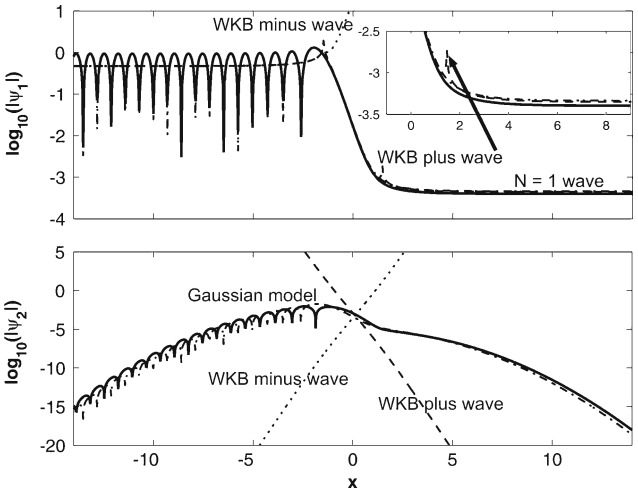

Fig. 8 Log plots of the wavefunction, specifically $\log_{10}|\psi_j|$, expressed in the adiabatic representation with respect to potential coupling, i.e., the representation intermediate between diabatic and $\psi_\pm$ representations. This, and all other wavefunctions shown below, were computed with $N_{\text{total}} = 10{,}000$ integration steps. The *top panel* corresponds to the lower channel of the two-level system, while the *bottom panel* corresponds to the upper channel. This is a below barrier energy eigenfunction ($E = 10$) for the potential A system, with $C_0 = 10$. The corresponding one-level system wavefunction is shown as a *dot-dashed line* in the top panel for comparison. The one and two-level wavefunctions are compared more closely in the inset of the top panel. Scaled WKB wavefunctions are also depicted in both panels. The WKB plus wave (right-going) and minus wave (left-going) are shown as *dashed* and *dotted lines*, respectively. In the bottom panel, a Gaussian model function (*dot-dashed line*) overlays the wavefunction, with close agreement except for a 90° phase shift

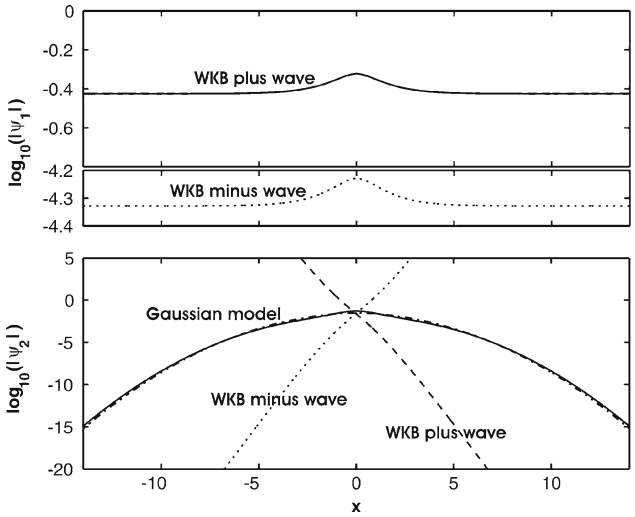

Fig. 9 As in Fig. 8 except $E = 25$ and the one-level system wavefunction is not shown in the top panel. The *top panel* has a split scale in order to accommodate the small variations in both the WKB plus and minus waves on the same graph. The amplitude of the WKB minus wave is chosen to match that of ψ_{2-}, the left-going component of the upper channel wavefunction (not shown) in the left asymptotic region, i.e., it gives the correct above-barrier reflection probability. Note that the computed wavefunction in the top panel exactly coincides with the WKB plus wave

energies. For the first resonance wavefunction (Fig. 10), the lower level wavefunction is modeled by $\varphi_+(x)+\varphi_-(x)$ up to about $x = -1$. Beyond this value the lower level wavefunction is non-adiabatic. Strictly speaking, this wavefunction is modeled by $\varphi_+(x)$—scaled down by about 10 orders of magnitude—for $x \gtrsim 5$. However, the amplitude of this very weak transmitted wave is sensitive to how accurately the resonance energy is determined. Figure 10 shows the first resonance wavefunction, with the resonance energy determined to double precision accuracy. The associated transmission probability is about 10^{-20}. In Fig. 11, three successively better converged fourth-resonance energies are chosen, showing how the transmission probability drops as the exact resonance energy is approached. The energies are 42.37954, 42.37953 and 42.3795273. Convergence of this resonance to double precision accuracy, 42.3795273343290, produces a transmission probability of about 10^{-21}.

There is traditionally little concern for the behavior of the wavefunction in closed channels. Most applications focus on reflection probabilities (or transmission probabilities as in Ref. [6]). Here, we look at the upper channel wavefunctions shown in the bottom panels of Figs. 8, 9, 10, 11 and 12. In each case, there is a profile which fits very well to a Gaussian (or a Gaussian plus a larger but narrower pseudo-bound resonance wavefunction, in the case of the resonance energies, Figs. 10 and 11). In the tunneling cases (Figs. 8 and 12) the upper channel wavefunction is well modeled as the product of the lower channel wavefunction and a Gaussian (the same Gaussian used for the potential coupling)—except that it is 90° out of phase and slightly broader. Effectively, a smooth tunneling probability step function is applied to the otherwise symmetric Gaussian profile. In addition, there is an interference pattern mirroring that of the lower channel wavefunction, except for the 90° phase shift. We see interference, in spite of the fact that the adiabatic solutions in a closed channel are non-oscillatory. Along with the tunneling right–left asymmetry, the left-going right-going interference of the lower channel is evidently imprinted on the upper channel wavefunction. The imprinting of the asymmetry is consistent with the observed lowering of transmission probability due to non-adiabatic transition, i.e., that non-adiabatic transition occurs primarily to the left of the interaction region is consistent with it contributing primarily to reflection. However, we have not ruled out the damping of transmission and concomitant enhancement of reflection being an interference phenomenon (as it is for resonances, see below). Consider, for example, that the upper channel wavefunction has approximately equal (except for a phase factor) + and − components (plots are not shown). Nevertheless, computations at energies above and below $E = 10$ show that the factor by which transmission probability is damped by the introduction of the

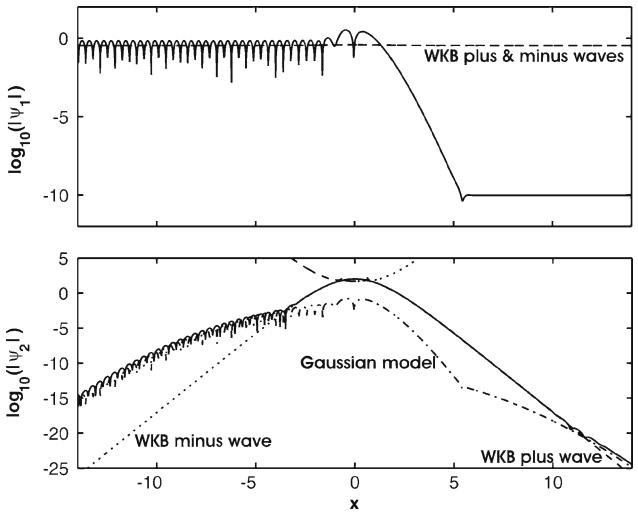

Fig. 10 As in Fig. 9 except $E = 36.3360539773469$ (the first resonance converged to double precision accuracy). For this energy, the left and right-going components of ψ_1 (i.e., ψ_{1+} and ψ_{1-}) have essentially the same amplitude. In this case, the WKB plus and minus waves shown overlap perfectly. Note the upper channel resonant wavefunction emerging from the Gaussian model background in the bottom panel. It is well modeled by the WKB waves—minus on the left and plus on the right

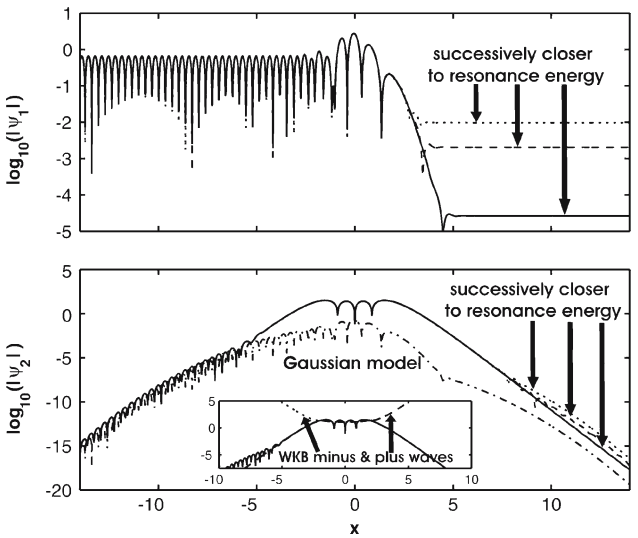

Fig. 11 As in Fig. 9 except $E = 42.37954$ (*dotted lines*), 42.37953 (*dashed lines*) and 42.3795273 (*solid lines*); i.e., three energies successively closer to the fourth resonance. The WKB waves are shown only in the inset of the bottom panel

upper channel varies little ($10^{-0.063 \text{ to } 0.061}$ for $E = 5$–12.5, respectively), while the amplitude of the upper channel wavefunction varies fivefold. It would seem the greater asymmetry of the upper channel wavefunction at lower energies compensates for the decreased amplitude of the non-adiabatic transition contribution to the overall scattering.

Computations (not shown) of the above-barrier wavefunctions (in $\psi_\pm$ representation) at energies above and below

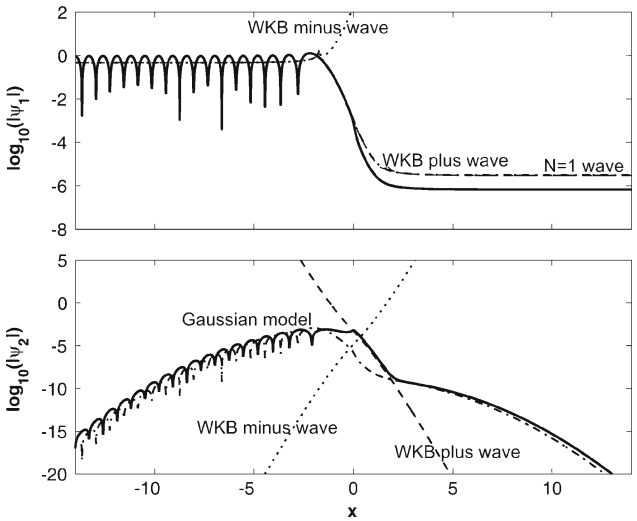

Fig. 12 As in Fig. 8 except this is the $E = 10$ energy eigenfunction for the tight avoided crossing potential A system $C_0 = 1$

$E = 25$, and for both $n = 1$ and $n = 2$, indicate that above-barrier reflection is enhanced by non-adiabatic transition. Because the upper level wavefunction is essentially symmetric in such cases (see the bottom panel of Fig. 9), this must be an interference effect (as it is for resonances, see below). The effect is much more sensitive to energy than the damping of tunneling transmission probability, especially as the bottom of the upper channel potential well is crossed. For example, the factor by which above-barrier reflection is enhanced increases from $10^{-0.02}$ to $10^{0.7}$ as E varies from 25 to 30.

The resonance energies wavefunctions are quite unlike neighboring energy wavefunctions which exhibit indiscernible (as in Fig. 9 which does not separate right and left-going contributions) exponentially small above-barrier reflection, and near 100% transmission. Right at resonance energies, reflection is near 100%. In the lower channel, the reflected wave interferes with the incoming wave to produce the pattern on the left—a small residual transmitted wave appears on the right. In the upper channel, we see the Gaussian-weighted imprint of the lower channel wavefunction (90° out of phase) plus another shape visible in an interval about $x = 0$. The latter shape is the pseudo-bound state in the upper channel which gives rise to the resonance. It does not have a Gaussian shape. Rather its tails, outside the classically allowed interval, fall-off exponentially because the upper channel potential is flat outside the interaction region. The tail on the right of the resonant bound state in Fig.10 shows an asymptotic linear (in the log plot) fall-off rather than the parabolic decay of the Gaussian profile. Note that three nodes are evident in the resonant portion of the upper channel wavefunction of Fig. 11, consistent with this being the third excited pseudo-bound state of the upper channel potential. There are no corresponding nodes in the ground state resonance of Fig. 10.

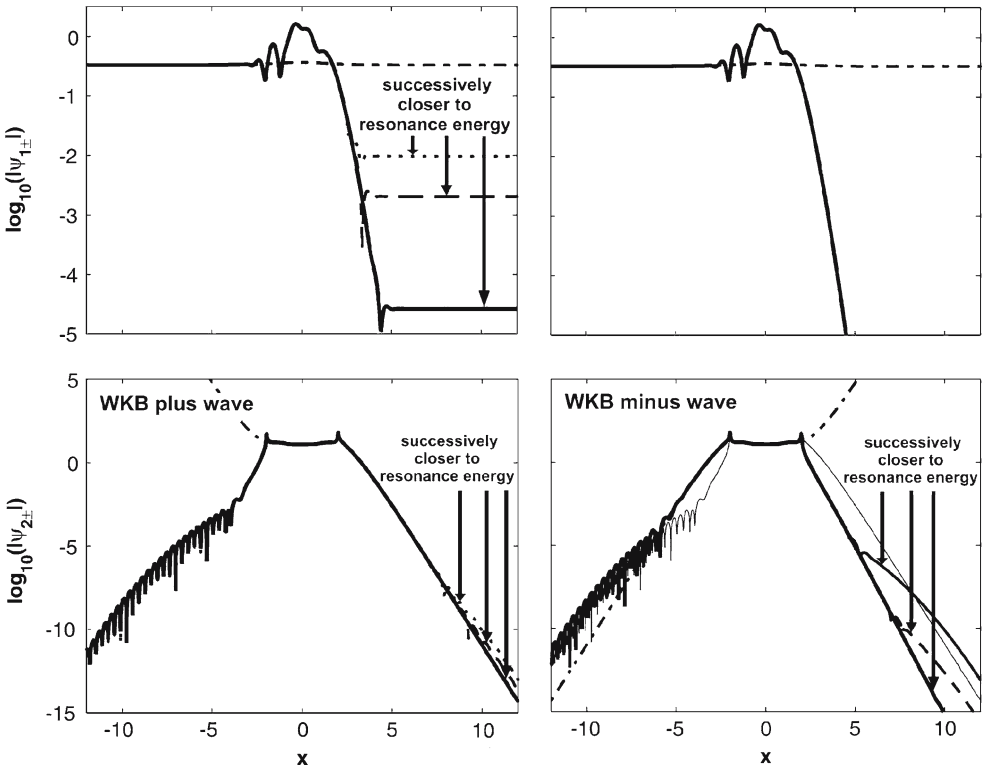

Fig. 13 The three successively more resonant wavefunctions of Fig. 11, shown here in $\psi_{\pm}$ representation—specifically, the right and left-going components, $\psi_{+}(x)$ (*right panels*) and $\psi_{-}(x)$ (*left panels*) respectively, of the fourth resonant wavefunction. From least to most resonant, the wavefunctions are shown as *dotted*, *dashed* and *solid lines*, respectively—as in Fig. 11. Note that the three wavefunctions differ only off the bottom of the graph in the *top right panel*. The WKB waves, $\varphi_{+}(x)$ and $\varphi_{-}(x)$ (in the *right* and *left panels*, respectively) are shown as *dot-dashed lines*. The thin line in the *bottom right panel* is just $\log_{10}|\psi_{2+}(x)|$, from the *bottom left panel*, reflected through $x = 0$

It is instructive to further examine resonant wavefunctions in adiabatic—i.e., $\psi_{\pm}$—representation, as provided in Fig. 13. Here, we see the right and left-going components of $\psi(x) = \psi_{+}(x) + \psi_{-}(x)$ at the fourth resonance energy. While the resonant portion of $\psi(x)$, in the upper channel, is symmetric about $x = 0$ (see lower panel Fig. 11), the associated right and left-going components are not. This is made clear by superimposing the resonant $\psi_{+}(x)$ (thin line in the bottom right panel) over the resonant $\psi_{-}(x)$ (thick line). The right-going component is larger to the right of the classically allowed interval. This portion of the wavefunction is exactly modeled by the WKB wavefunction, $\varphi_{+}(x)$, weighted to give the best match. The larger left portion of the left-going component is exactly modeled in the same fashion by $\varphi_{-}(x)$. This asymmetry is no surprise. Within the classically allowed interval we have a standing wave—an equal superposition of right and left-going waves (i.e., the two WKB waves). Outside the classically allowed interval, only the exponentially decaying WKB waves are seen—$\varphi_{+}(x)$ on the right and $\varphi_{-}(x)$ on the left. In any case, because $\varphi_{+}(x)$ and $\varphi_{-}(x)$ are right and left-going waves, respectively, within the classically allowed region as the turning point is crossed, it is convenient to think of these as right and left-going waves for all x. The asymmetry of the resonant states looks like a position-momentum asymmetry. It is as though the left (right)-going component pushes further into the left (right) unallowed region. Turning our attention to the lower channel wavefunctions, we see non-adiabaticity at and beyond the onset of the resonant wave. This non-adiabatic component of the lower level wavefunction can be modeled in terms of the upper channel wavefunction in a fashion similar to how we modeled the non-adiabatic component of the upper channel wavefunction in terms of the lower channel, i.e., the lower channel wavefunction looks like the product of a Gaussian (the potential coupling) and the upper channel resonant wavewith a 90° phase shift. This is in contrast to the adiabaticity of the lower channel wavefunction at non-resonant energies ($E = 10$ and 25 in Figs. 8 and 9). For $E = 10$, the right-going component (not shown) is adiabatic across the interval, while the left-going component (also not shown) is adiabatic only up to the first turning point in the lower channel.

The most important consequence of the resonant states is that they give rise to 100% reflectivity. The importance arises

because of the possibility of constructing nano-devices incorporating switches based on 100% reflectivity at resonance (see Chap. 12 of Ref. [29]). Near 100% reflectivity is also seen at any above-barrier energy of the tight avoided crossing case (see Fig. 6). The latter cases exhibit high reflectivity because they are near the diabatic limit where transmission is impossible—the incoming wave sees only a repulsive wall on the right. The resonant wave results in 100% reflectivity because, at resonance, the incoming wave splits into the resonant wave (in the upper channel) and a direct transmitting wave in the lower channel, such that the indirect transmitting wave emerging from the resonant state exactly cancels the transmitting wave resulting directly from the incoming wave to give zero net transmission (see Chap. 11 of Ref. [29]). Note that the resonant wave leaks out of the upper channel very slowly, equally in both directions, so that the amplitude of the indirect transmitting and reflecting waves in the lower channel is much smaller than the resonant wave. The amplitude of the indirect transmitting and reflecting waves exactly matches that of the incoming wave and the direct transmitting wave, with the two transmitting waves out-of-phase, right at resonance.

Interference between a non-resonant continuum and a resonance gives rise to a Fano resonance [37,38] profile which can exhibit zero net transmission.[5] Nakamura has proposed that a series of two-level avoided crossings, exhibiting bands of 100% reflection, could be used as a switch through control of the electron energy. Bands of reflection resonances are analogous to the bands of transmission resonances (at below barrier energies) of a series of barriers in a one-level system. In Ref. [40], it is shown that to get true band of near 100% transmission, one must bracket a series of identical barriers with smaller barriers—an anti-reflective coating. Otherwise, a set of discrete narrow transmission resonances is seen.

The non-resonant upper channel wavefunction (and "non-resonant" portion of the upper channel wavefunction at resonance) is a quandary for semiclassical mechanics. For example, in Fig. 8, the WKB wavefunctions $\varphi_{\pm}(x)$ (weighted to match $\psi(x)$ at $x = 0$) in the upper channel are much steeper than the observed Gaussian profile. The upper channel wavefunction is highly non-adiabatic, and as such much broader than one might expect, i.e., naively assuming the adiabaticity of the lower channel wavefunction applies to the upper channel. In a strict sense, the Gaussian profile represents the failure of the semiclassical approximation. However, it is shown in Ref. [41] that the Gaussian profile is recovered with a generalization of the WKB semiclassical approximation. In particular, the non-resonant upper channel wavefunction arises from $\mathsf{Z}'(x)$. As such, it is closely related to the profile of the potential coupling which is the principle source of variation in the diabatic to adiabatic transformation matrix, $\mathsf{Z}(x)$. Here, the relationship between the potential coupling and the upper channel wavefunction is investigated empirically by varying the functional form of the coupling. Figure 14 shows the upper channel wavefunctions for $E = 10$, with the Gaussian potential coupling replaced by a Lorentzian of the same height and width (bottom two panels), and a constant coupling (top panel). $C_0 = 10$ for both potential models. The three panels of Fig. 14 compare with the bottom panel of Fig. 8 which shows the corresponding Gaussian-coupling upper channel wavefunction. The model for the upper channel shown in the top two panels of Fig. 14 (dot-dashed lines) is given by multiplying the lower channel wavefunction by the potential coupling—just like the Gaussian model shown in Fig. 8. The Gaussian model is a little narrower than the observed upper channel wavefunction. For constant and Lorentzian coupling (top two panels of Fig. 14), the model provides a broader profile than the observed wavefunctions, especially in the constant coupling case. Of course, the model in the constant coupling case is not a good model for $\mathsf{Z}'(x)$. It is shown here for comparison purposes only. The observed profile in the constant coupling case is simple exponential decay to the left and right. In the case of Lorentzian coupling, another model wavefunction is considered—the absolute value of the derivative of the

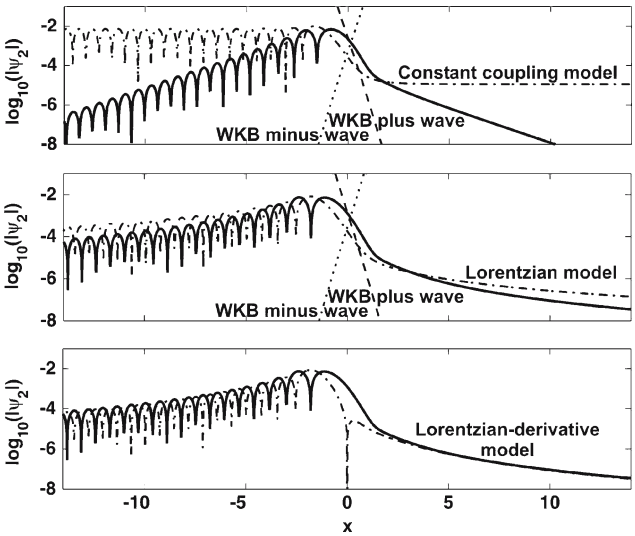

Fig. 14 The upper channel wavefunctions for $E = 10$, with the Gaussian potential coupling replaced by a constant (*top panel*), and a Lorentzian of the same height and width (*bottom two panels*). $C_0 = 10$ for both potential models. Model upper channel wavefunctions are shown as *dot-dashed lines*. In the *top two panels*, the model is just the product of the lower channel wavefunction and the potential coupling (scaled to give the best fit). In the *bottom panel*, the derivative of the Lorentzian coupling (with width reduced to 2) is used instead of the Lorentzian coupling (middle panel). WKB plus (*dashed lines*) and minus (*dotted lines*) are shown for comparison

[5] For a recent observation of Fano resonance giving rise to zero net transmission in mesoscopic transport, see Ref. [39].

Lorentzian coupling (with the width reduced to 2, i.e., as opposed to 2.5, the width of the coupling used in the wavefunction computation) multiplying the lower level wavefunction. This latter model, shown in the bottom panel, fits exceptionally well.

5 Summary

A new numerical method, the shift equations iteration, is introduced to solve n-level close coupled equations without exponential instability. It is shown that exponential growth accrued between grid points in the propagation is eliminated in passing to the next grid point spacing. Stability is ensured if there are sufficiently many grid points—around 20 in the two-level avoided crossing systems considered above. The numerical results show that SEI can be very efficient when combined with an efficient underlying integrator. In fact, results show that SEI simply reflects the error in the underlying integrator—the error depends only on the total number of underlying integrator steps and not on the number of SEI grid points. Rapid convergence is obtained with the symplectic log-derivative method of Manolopoulos and Gray [25], based on the McLachlan Atela [26] fifth order symplectic integrator. Convergence obtained with SEI is comparable to that obtained by Alexander et al. [6], using the Manolopoulos [10] log-derivative method, and better than that obtained using the original Johnson [7] log-derivative method. In addition to providing numerical efficacy, SEI offers exponential-divergence-free computation of transmission and reflection coefficients, and accurate wavefunctions for one or two-sided systems. It is not clear whether log-derivative methods can be adapted to provide accurate wavefunctions, including closed channel components, for general two-sided n-level systems.

SEI is interpreted as an effective propagation across the interval, starting in the incoming channel, then traversing back again. This effective propagation which suppresses exponential instability is represented schematically in Figs. 1 and 2. SEI replaces a boundary value problem by an initial value problem in the forward direction, followed by another initial value problem in the backward direction. This is just what was achieved by Ridley [42] in 1956. In fact, the key to Ridley's recast of the one-dimensional Schrödinger equation is a matrix LU decomposition (in one of the formulations described in Ref. [42]), as it is for ours.

Numerical results for two-level single avoided crossing models show a range of phenomena. Most notably, resonances in the upper channel well appear as negative peaks in transmission probability with apparently zero probability exactly at resonance, as seen by Zhu and Nakamura [27]. Also, at non-resonant as well as resonant energies, the upper channel wavefunction exhibits a broad background distribution (in superposition with a resonant wave at resonant energies) which is empirically modeled as the product of the lower channel wavefunction (phase shifted by 90°) and the diabatic potential coupling (or a variation thereof). The broad background distribution is not describable in terms of WKB functions—it is much broader. The resonant wave, appearing only near resonance energies, is so describable. The latter exhibits exponential decay in accordance with WKB functions to the left and right of the upper channel classically allowed interval. While the broad background distribution is generally small, it may in any case play an important role in the interaction between neighboring avoided crossings because of its breadth.

Acknowledgments The authors thank Reza R. Khorasani for helpful discussions on integrators, especially the Verlet and log-derivative methods, and the Natural Sciences and Engineering Research Council of Canada for financial support.

Appendix: LU solution of the shift equations

Equation (16) is solved via LU decomposition of its block quadridiagonal coefficient matrix, written here as

$$\mathsf{LU} = \begin{pmatrix} -\mathsf{L}^{(1)}_{+-} & & & & & & \\ -\mathsf{L}^{(1)}_{--} & -\Lambda^{(1)}_{-+} & & & & & \\ & -\mathsf{L}^{(2)}_{++} & -\mathsf{L}^{(2)}_{+-} & & & & \\ & -\mathsf{L}^{(2)}_{-+} & -\mathsf{L}^{(2)}_{--} & -\Lambda^{(2)}_{-+} & & & \\ & & \ddots & \ddots & & & \\ & & & & -\mathsf{L}^{(N)}_{++} & -\mathsf{L}^{(N)}_{+-} & \\ & & & & -\mathsf{L}^{(N)}_{-+} & -\mathsf{L}^{(N)}_{--} & -\Lambda^{(N)}_{-+} \end{pmatrix} \times \begin{pmatrix} 1 & -\mathsf{U}^{(1)}_{-+} & & & & & \\ & 1 & -\mathsf{U}^{(1)}_{+-} & & & & \\ & & 1 & -\mathsf{U}^{(2)}_{-+} & & & \\ & & & 1 & -\mathsf{U}^{(2)}_{+-} & & \\ & & & & \ddots & \ddots & \\ & & & & & 1 & -\mathsf{U}^{(N)}_{-+} \\ & & & & & & 1 \end{pmatrix}$$

$$= \begin{pmatrix} -\mathsf{L}^{(1)}_{+-} & \mathsf{L}^{(1)}_{+-}\mathsf{U}^{(1)}_{-+} & & & & & & \\ -\mathsf{L}^{(1)}_{--} & \mathsf{L}^{(1)}_{--}\mathsf{U}^{(1)}_{-+} - \Lambda^{(1)}_{-+} & \Lambda^{(1)}_{-+}\mathsf{U}^{(1)}_{+-} & & & & & \\ & -\mathsf{L}^{(2)}_{++} & \mathsf{L}^{(2)}_{++}\mathsf{U}^{(1)}_{+-} - \mathsf{L}^{(2)}_{+-} & \mathsf{L}^{(2)}_{+-}\mathsf{U}^{(2)}_{-+} & & & & \\ & -\mathsf{L}^{(2)}_{-+} & \mathsf{L}^{(2)}_{-+}\mathsf{U}^{(1)}_{+-} - \mathsf{L}^{(2)}_{--} & \mathsf{L}^{(2)}_{--}\mathsf{U}^{(2)}_{-+} - \Lambda^{(2)}_{-+} & \Lambda^{(2)}_{-+}\mathsf{U}^{(2)}_{+-} & \ddots & & \\ & & & \ddots & \ddots & \ddots & & \\ & & & & \ddots & -\mathsf{L}^{(N)}_{++} & \mathsf{L}^{(N)}_{++}\mathsf{U}^{(N-1)}_{+-} - \mathsf{L}^{(N)}_{+-} & \mathsf{L}^{(N)}_{+-}\mathsf{U}^{(N)}_{-+} \\ & & & & & -\mathsf{L}^{(N)}_{-+} & \mathsf{L}^{(N)}_{-+}\mathsf{U}^{(N-1)}_{+-} - \mathsf{L}^{(N)}_{--} & \mathsf{L}^{(N)}_{--}\mathsf{U}^{(N)}_{-+} - \Lambda^{(N)}_{-+} \end{pmatrix}$$

Identifying the product of the L and U matrices with the original coefficient matrix, starting at the top left corner, provides the explicit form of the L and U blocks (see below). In terms of L and U, the system of equations is solved in two parts. First we solve

$$\begin{pmatrix} -\mathsf{L}^{(1)}_{+-} & & & & & & & \\ -\mathsf{L}^{(1)}_{--} & -\Lambda^{(1)}_{-+} & & & & & & \\ & -\mathsf{L}^{(2)}_{++} & -\mathsf{L}^{(2)}_{+-} & & & & & \\ & -\mathsf{L}^{(2)}_{-+} & -\mathsf{L}^{(2)}_{--} & -\Lambda^{(2)}_{-+} & & & & \\ & & & \ddots & \ddots & & & \\ & & & & -\mathsf{L}^{(N)}_{++} & -\mathsf{L}^{(N)}_{+-} & & \\ & & & & -\mathsf{L}^{(N)}_{-+} & -\mathsf{L}^{(N)}_{--} & -\Lambda^{(N)}_{-+} & \end{pmatrix} \times \begin{pmatrix} \mathbf{b}^{(0)}_{-} \\ \mathbf{b}^{(1)}_{+} \\ \mathbf{b}^{(1)}_{-} \\ \mathbf{b}^{(2)}_{+} \\ \vdots \\ \mathbf{b}^{(N-1)}_{-} \\ \mathbf{b}^{(N)}_{+} \end{pmatrix} = \begin{pmatrix} \mathsf{F}^{(1)}_{++}\mathbf{c}^{(0)}_{+} \\ \mathsf{F}^{(1)}_{-+}\mathbf{c}^{(0)}_{+} \\ 0 \\ 0 \\ \vdots \\ 0 \\ 0 \end{pmatrix}, \tag{25}$$

then solve

$$\begin{pmatrix} 1 & -\mathsf{U}^{(1)}_{-+} & & & & & & \\ & 1 & -\mathsf{U}^{(1)}_{+-} & & & & & \\ & & 1 & -\mathsf{U}^{(2)}_{-+} & & & & \\ & & & \ddots & \ddots & & & \\ & & & & 1 & -\mathsf{U}^{(N-1)}_{+-} & & \\ & & & & & 1 & -\mathsf{U}^{(N)}_{-+} & \\ & & & & & & 1 & \end{pmatrix} \begin{pmatrix} \mathbf{c}^{(0)}_{-} \\ \mathbf{c}^{(1)}_{+} \\ \mathbf{c}^{(1)}_{-} \\ \mathbf{c}^{(2)}_{+} \\ \vdots \\ \mathbf{c}^{(N-1)}_{-} \\ \mathbf{c}^{(N)}_{+} \end{pmatrix} = \begin{pmatrix} \mathbf{b}^{(0)}_{-} \\ \mathbf{b}^{(1)}_{+} \\ \mathbf{b}^{(1)}_{-} \\ \mathbf{b}^{(2)}_{+} \\ \vdots \\ \mathbf{b}^{(N-1)}_{-} \\ \mathbf{b}^{(N)}_{+} \end{pmatrix}.$$

In practice, the L system of equations are solved concurrently with the construction of the L and U components.

So far, the method is straightforward. However, following the usual construction of the L and U components, $\mathsf{U}^{(j)}_{-+}$ blocks are given as the inverse of the $\mathsf{L}^{(j)}_{+-}$ blocks. This is a problem because the latter blocks are vanishingly small in the asymptotic regions. They are effective propagators—closely related to $\mathsf{F}^{(j)}_{+-}$ (see Eq. (27) below)—mapping minus components at x_{j-1} to plus components at x_j. As such, they vanish in asymptotic regions where there are no such transitions. $\mathsf{U}^{(j)}_{-+}$ is consequently ill defined, as is $\mathbf{b}^{(j)}_{-}$ which is expressed in terms of $\left(\mathsf{L}^{(j+1)}_{+-}\right)^{-1}$ following the usual prescription for solving the system of equations via LU decomposition. It is, however, possible to express the final solution, $\mathbf{c}$, only in terms of the $+$ components, $\mathbf{b}^{(j)}_{+}$, of the intermediate solution and the blocks of L, i.e., with no reference to $\mathsf{U}^{(j)}_{-+}$. The resulting solution to the system of equations provides the promised numerically viable strategy, with the additional advantage of a graphical interpretation of the solution as an evolution across the interval and back.

With the conventions, $\mathsf{L}^{(0)}_{\pm-} = 0$ and $\mathsf{L}^{(1)}_{\pm+} = \mathsf{F}^{(1)}_{\pm+}$, the equations for the blocks of L can be written concisely as

$$\mathsf{L}^{(j)}_{\pm+} = \mathsf{F}^{(j)}_{\pm+}, \quad j = 1, \ldots, N, \tag{26}$$

and

$$\begin{aligned} \mathsf{L}^{(j)}_{\pm-} &= \mathsf{F}^{(j)}_{\pm-} + \mathsf{L}^{(j)}_{\pm+}\mathsf{U}^{(j-1)}_{+-} \\ &= \mathsf{F}^{(j)}_{\pm-} + \mathsf{F}^{(j)}_{\pm+}\mathsf{L}^{(j-1)}_{+-}\left(\mathsf{L}^{(j-1)}_{--}\right)^{-1}, \quad j = 1, \ldots, N. \end{aligned} \tag{27}$$

The second line of Eq. (27) follows from $\mathsf{U}^{(j)}_{+-} = \left(\Lambda^{(j)}_{-+}\right)^{-1}$, $\Lambda^{(j)}_{-+} = \mathsf{L}^{(j)}_{--}\mathsf{U}^{(j)}_{-+}$, $\mathsf{U}^{(j)}_{-+} = \left(\mathsf{L}^{(j)}_{+-}\right)^{-1}$ and Eq. (26). These equations show how the blocks of L can be viewed as effective propagators (L-propagators) between neighboring points. The mappings, $\mathsf{L}^{(j)}_{\pm+}$, from $+$ components at x_{j-1} to $\pm$ components at x_j are just the elementary mappings, $\mathsf{F}^{(j)}_{\pm+}$. The mappings, $\mathsf{L}^{(j)}_{\pm-}$, from $-$ components have a term in addition to the elementary mapping, $\mathsf{F}^{(j)}_{\pm-}$. The extra term corresponds to

L-propagation to $-$ components at x_{j-2} followed successively by L-propagation to $+$ components at x_{j-1} and F-propagation to $\pm$ components at x_j. The two terms in Eq. (27) can be viewed as corresponding to two distinct pathways from $-$ components at x_{j-1} to $\pm$ components at x_j. This interpretation is illustrated schematically in Fig. 1 which depicts the $\mathsf{L}^{(j)}_{\pm-}$ as solid arrows which map $-$ components at x_{j-1} (the solid square) to $+$ and $-$ components at x_j (the top and bottom open squares, respectively). Each of these mappings is constructed from two pathways depicted by dashed lines—medium and short dashed arrows correspond to $\mathsf{L}^{(j)}_{--}$ and $\mathsf{L}^{(j)}_{+-}$ contributions, respectively. In each case there is a direct path contribution—the $\mathsf{F}^{(j)}_{\pm-}$—and an indirect contribution. The first two steps of the indirect contributions are the same for $\mathsf{L}^{(j)}_{--}$ and $\mathsf{L}^{(j)}_{+-}$—they are indicated with long dashed arrows. This shared portion of the indirect pathways consists of the mappings, $\left(\mathsf{L}^{(j-1)}_{--}\right)^{-1}$ and $\mathsf{L}^{(j-1)}_{+-}$, which are in turn expressed in terms of direct and indirect contributions in the previous iteration of Eq. (27).

The equations for the intermediate solution, $\mathbf{b}^{(j)}_+$, can also be written in concise fashion—via the convention, $\mathbf{b}^{(0)}_+ = \mathbf{c}^{(0)}_+$, the incoming seed wave on the left. Starting with

$$\begin{aligned}\mathbf{b}^{(j)}_+ &= -\left(\Lambda^{(j)}_{-+}\right)^{-1}\left[\mathsf{L}^{(j)}_{--}\mathbf{b}^{(j-1)}_- + \mathsf{L}^{(j)}_{-+}\mathbf{b}^{(j-1)}_+\right] \\ &= -\mathsf{L}^{(j)}_{+-}\left[\mathbf{b}^{(j-1)}_- + \left(\mathsf{L}^{(j)}_{--}\right)^{-1}\mathsf{L}^{(j)}_{-+}\mathbf{b}^{(j-1)}_+\right], \quad j = 1,\ldots,N,\end{aligned}$$

and

$$\mathbf{b}^{(j-1)}_- = -\left(\mathsf{L}^{(j)}_{+-}\right)^{-1}\mathsf{L}^{(j)}_{++}\mathbf{b}^{(j-1)}_+, \qquad j = 1,\ldots,N,$$

we eliminate $\mathbf{b}^{(j-1)}_-$ to get

$$\begin{aligned}\mathbf{b}^{(j)}_+ &= \left[\mathsf{L}^{(j)}_{++} - \mathsf{L}^{(j)}_{+-}\left(\mathsf{L}^{(j)}_{--}\right)^{-1}\mathsf{L}^{(j)}_{-+}\right]\mathbf{b}^{(j-1)}_+ \\ &= \left[\mathsf{F}^{(j)}_{++} - \mathsf{L}^{(j)}_{+-}\left(\mathsf{L}^{(j)}_{--}\right)^{-1}\mathsf{F}^{(j)}_{-+}\right]\mathbf{b}^{(j-1)}_+, \quad j = 1,\ldots,N.\end{aligned} \tag{28}$$

The $\mathbf{b}^{(j)}_+$ emerge from successive plus to plus propagations across the interval, starting with $\mathbf{c}^{(0)}_+$ for $j = 1$. Each step has two contributions, a plus to plus L-propagation of $\mathbf{b}^{(j-1)}_+$ from x_{j-1} to x_j, and a three stage L-propagation mapping plus at x_{j-1} to minus at x_j, then to minus at x_{j-1} and finally to plus at x_j. The second contribution is subtracted from the first. The second contribution can be viewed as the mapping of minus components at x_{j-1} via minus to plus L-propagation. The minus components at x_{j-1} are chosen such that their minus to minus L-propagation to x_j cancels the plus to minus L-propagation of $\mathbf{b}^{(j-1)}_+$ from x_{j-1} to x_j.

We can now solve the equations for the $\mathbf{c}^{(j)}_\pm$. The associated equations are concisely expressed via

$$\begin{aligned}\mathbf{c}^{(j)}_+ &= \mathbf{b}^{(j)}_+ + \mathsf{U}^{(j)}_{+-}\mathbf{c}^{(j)}_- \\ &= \mathbf{b}^{(j)}_+ + \mathsf{L}^{(j)}_{+-}\left(\mathsf{L}^{(j)}_{--}\right)^{-1}\mathbf{c}^{(j)}_-, \quad j = N,\ldots,1,\end{aligned} \tag{29}$$

and

$$\begin{aligned}\mathbf{c}^{(j-1)}_- &= \mathbf{b}^{(j-1)}_- + \mathsf{U}^{(j)}_{-+}\mathbf{c}^{(j)}_+ \\ &= \left(\mathsf{L}^{(j)}_{+-}\right)^{-1}\left[-\mathsf{L}^{(j)}_{++}\mathbf{b}^{(j-1)}_+ + \mathbf{b}^{(j)}_+ + \mathsf{L}^{(j)}_{+-}\left(\mathsf{L}^{(j)}_{--}\right)^{-1}\mathbf{c}^{(j)}_-\right] \\ &= \left(\mathsf{L}^{(j)}_{+-}\right)^{-1}\left[-\mathsf{L}^{(j)}_{++}\mathbf{b}^{(j-1)}_+ + \left[\mathsf{L}^{(j)}_{++} - \mathsf{L}^{(j)}_{+-}\left(\mathsf{L}^{(j)}_{--}\right)^{-1}\mathsf{L}^{(j)}_{-+}\right]\right. \\ &\qquad \left.\times\,\mathbf{b}^{(j-1)}_+ + \mathsf{L}^{(j)}_{+-}\left(\mathsf{L}^{(j)}_{--}\right)^{-1}\mathbf{c}^{(j)}_-\right] \\ &= \left(\mathsf{L}^{(j)}_{--}\right)^{-1}\left[\mathbf{c}^{(j)}_- - \mathsf{F}^{(j)}_{-+}\mathbf{b}^{(j-1)}_+\right], \quad j = N,\ldots,1.\end{aligned} \tag{30}$$

Equation (29) shows the $+$ components, $\mathbf{c}^{(j)}_+$, of the energy eigenfunction to consist of $\mathbf{b}^{(j)}_+$ plus a term corresponding to $-$ to $-$ L-propagation of $\mathbf{c}^{(j)}_-$ from x_j to x_{j-1}, followed by $-$ to $+$ L-propagation back to x_j. The boundary condition, $\mathbf{c}^{(N)}_- = \mathbf{0}$ allows Eq. (29) to be applied first for each j from N down to 1. The transmission coefficients are consequently contained in the bottom $\mathbf{b}_+$ block, $\mathbf{b}^{(N)}_+$; i.e.,

$$\mathbf{T} = \mathbf{c}^{(N)}_+ = \mathbf{b}^{(N)}_+. \tag{31}$$

The reflection coefficients appear as

$$\mathbf{R} = \mathbf{c}^{(0)}_-. \tag{32}$$

The $-$ components, $\mathbf{c}^{(j-1)}_-$, of the energy eigenfunction correspond to successive L-propagations across the interval from right to left. However, at each point, x_{j-1}, a term is subtracted out—specifically, the $-$ components at x_{j-1}, mentioned above, which are such that their $-$ to $-$ L-propagation to x_j cancels the $+$ to $-$ L-propagation of $\mathbf{b}^{(j-1)}_+$ from x_{j-1} to x_j. The propagation of $\mathbf{b}^{(j)}_+$, $\mathbf{c}^{(j)}_+$ and $\mathbf{c}^{(j-1)}_-$ according to Eqs. (28), (29) and (30) is represented schematically in Fig. 2. System states appear as boxes, with named states labeled. Each state (except the initial seed state, $\mathbf{c}^{(0)}_+$) is a sum of contributions represented by arrows, labeled by the associated mapping, pointing to the box. Dashed arrows in this figure correspond to the identity mapping. Here we see the solution of the Schrödinger equation depicted as a propagation from left to right, starting with the seed state, followed by propagation back to the left. The transmission and reflection coefficients appear as end states on the right and left, respectively.

References

1. Nyman G, Yu H-G (2000) Rep Prog Phys 63:1001
2. Laing JR, George TF (1977) Phys Rev A 16:1082 and references therein
3. Walker RB, Light JC (1976) J Chem Phys 64:4272
4. Stechel EB, Walker RB, Light JC (1978) J Chem Phys 69:3518
5. Alexander MH, Manolopoulos DE (1987) J Chem Phys 86:2044
6. Alexander MH, Parlant G, Hemmer TH (1989) J Chem Phys 91:2388
7. Johnson B (1973) J Comput Phys 13:445
8. Mrugala F, Secrest D (1983) J Chem Phys 78:5954
9. Mrugala F, Secrest D (1983) J Chem Phys 79:5960
10. Manolopoulos DE (1986) J Chem Phys 85:6425
11. Child MS (1996) Molecular collision theory. Dover, Mineola
12. Bačić Z, Kress JD, Parker GA, Pack RT (1990) J Chem Phys 92:2344
13. Bodo E, Gianturco FA, Dalgarno A (2002) J Chem Phys 116:9222
14. Manolopoulos DE (1997) J Chem Soc Faraday Trans 93:673
15. Echave J (1996) J Chem Phys 104:1380
16. Abrashkevich DG, Brumer P (2001) J Chem Phys 114:54
17. Gianturco FA, Materzanini G (1999) Phys Rev A 60:1165
18. Heath JR, Ratner MA (2003) Phys Today 56:43
19. Nitzan A, Ratner MA (2003) Science 300:1384
20. Sánchez CG, Stamenova M, Sanvito S, Bowler DR, Horsfield AP, Todorov TN (2006) J Chem Phys 124:214708–1
21. Li J, Wang L-W (2005) Phys Rev B 72:125325
22. Landauer R (1957) IBM J Res Dev 1:223
23. Nitzan A (2001) Annu Rev Phys Chem 52:681
24. Lam SWK, Dumont RS (unpublished work)
25. Manolopoulos DE, Gray SK (1995) J Chem Phys 102:9214
26. McLachlan RI, Atela P (1991) Nonlinearity 5:541
27. Zhu C, Nakamura H (1994) J Chem Phys 101:10630
28. Zhu C, Nakamura H (1993) J Chem Phys 98:6208
29. Nakamura H (2002) Nonadiabatic transition. World Scientific, Singapore
30. Dumont RS, Pechukas P (1988) J Chem Phys 89:5764
31. von Neumann J, Wigner E (1929) Phys Z 30:467
32. Eu BC (1984) Semiclassical theories of molecular scattering. Springer-Verlag, Berlin
33. Reed M, Simon B (1980) Methods of modern mathematical physics I: functional analysis. Academic, New York
34. Feschbach H (1958) Ann Phys (NY) 5:363
35. Feschbach H, Nenciu G (1991) Rev Mod Phys 63:91
36. Dumont RS (2002) J Chem Phys 116:9158
37. Fano U (1961) Phys Rev 124:1866
38. Fano U, Rau ARP (1986) Atomic collision and spectra. Academic, Orlando
39. Voo K-K, Chu CS (2005) Phys Rev B 72:165307 and references therein
40. Veenstra CN, van Dijk W, Sprung DWL, Martorell J, arxiv:cond-mat/0411118
41. Dumont RS, Lam SWK, unpublished work
42. Ridley EC (1957) Proc Camb Phil Soc 53:442